Investigating the Ride Properties of a Particle Filled Wheel for Planetary Mobility

Daniel A. Oyama

Master of Engineering

Department of Mechanical Engineering

McGill University

Montreal,Quebec

December 14, 2013

A Thesis submitted to the Faculty of Graduate studies in partial fulfilment of the degree of Master of Engineering

DEDICATION

To my first teachers, Mordechai and Kasey.

ACKNOWLEDGEMENTS

I would like to thank my supervisors Peter Radziszewski and Jozsef Kovecses for the guidance and support they provided me throughout my time at McGill.

A special thanks is due to my friend and colleague Sudarshan Martins for being beside me every step of the way.

I must also acknowledge Brad Jones, Mo Farhat, Michele Faragalli, Gary Savard, John Boisvert, Mike Mizrahi, Chris Jackson for sharing their expertise, resources and time.

Finally, I thank my family and friends for their love, support, patience and understanding.

ABSTRACT

Ride is the isolation of passenger and cargo from terrain inputs on a moving vehicle. While most lunar rover designs assign this duty to shock absorbers, Dr Peter Radziszewski and Dr Sudarshan Martins propose it be supplied in larger part by the wheels. Their invention, dubbed iRings, consists of a 24 inch diameter chainmail tire carcass filled with thousands of polypropylene spheres. When spun beyond a *critical speed*, their centripetal acceleration compresses them against the chain-mail, which lacking any structure, adopts their bulk stiffness, damping and shape. In this thesis, measurements of iRings' free response to an impulse while spinning are analysed to create a linear single degree of freedom contact model. The model's damping ratio drops from 0.8-0.9 at 0 rpm to 0.01 at 131 rpm as both its stiffness and damping decrease with speed. The transition occurs close to the Davis critical speed of 54 rpm. Throughout, natural frequency remains constant at 3-4 Hz despite large fluctuations in stiffness. This is likely because iRings oscillates as a result of plastic and not elastic deformation. This model is matched in-silico to the Canadian Space Agency's (CSA) rovers Juno and Artemis and the whole is tested on a sinusoidal lunar analogue terrain supplied by the CSA. The iRings wheel is found to supply comparable, but slightly inferior isolation than a pneumatic tire, the Carlisle AT-489. Nevertheless, iRings proves itself to be a passively adaptive suspension component and with improvements to its stiffness, could surpass the pneumatic wheel.

ABRÉGÉ

Le comfort des passagers et cargo d'une vhicule consiste de l'isolation qu'il fournisse du terrain sur lequel il se dplace. Alors que la plupart des vhicules lunaires comblent ce besoin avec des absorbeur de chocs, Dr Peter Radziszewski et Dr Sudarshan Martins proposent que les roues prennent encore plus la relve. Leur invention, surnomm iRings, consiste d'une enveloppe en cote de mail remplie de miliers de sphres en polypropylne. Lorsqu'elles se font tourner au dl d'une *vitesse critique*, les sphres font une pression sure le cote de mail qui, ayant aucune structure, adopte leur amortissement, rigidit et forme. Dans cette thse, la mesure de la raction naturelle une impulsion d'une roue iRings en train de tourner est analyse pour crer une systme linaire un seule degr de libert reprsentative de son contact. Son rapport d'amortissement descends de 0.8-0.9 0 tour par minute (tpm) jusqu' 0.01 131 tpm du au fait que son amortissement et rigidit diminuent avec la vitesse. La transition se manifeste autour de la vitesse criticale Davis de 54 tpm. Tout au long, sa frquence naturelle reste entre 3-4 Hz malgr des fluctuations importantes de rigidit. La fait qu'iRings se trouve a osciller cause de dformation plastique et non lastique. Ce modle est intgre in silico avec Juno et Artemis, voitures lunaires de l'Agence Spatiale Canadienne (ASC), et par la suite le tout est excite par une surface sinusoidale spcifie par l'ASC. La roue iRings fournisse une isolation similaire cependant infrieure une roue pneumatique, le Carlisle AT-489. Nanmoins, iRings prouve qu'elle peut servir d'amortisseur auto-adaptif et qu'avec quelques amliorations sa rigidite, pourrait surpasser la roue pneumatique.

TABLE OF CONTENTS

LIST OF TABLES

LIST OF FIGURES

CHAPTER 1
Introduction and Research Objectives

1.1 Ad Astra

Consumer vehicle design is iterative by nature and conservative by necessity.

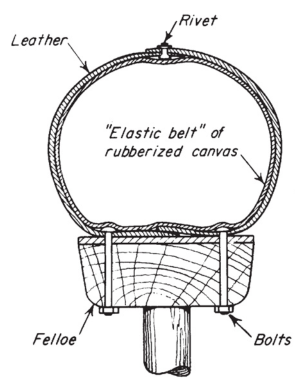

(a) The first pneumatic tire (1845) [1]

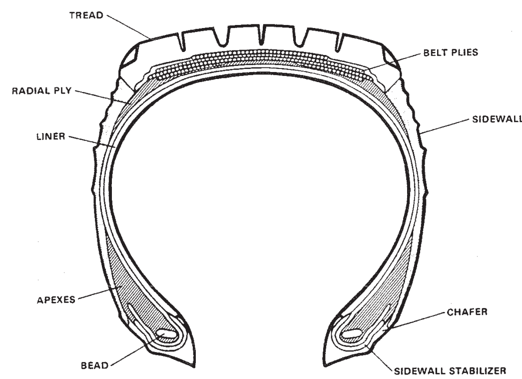

(b) The radial ply tire [2]

Figure 1–1: The evolution of pneumatic tire design

The pneumatic tire, invented in 1845 by Thomson, and a modern radial tire placed side by side speak to a subtle evolution as opposed to radical change. Thomson's pressurized inner tube was never replaced, it was built upon. In stark contrast to this tradition lies the field of extra-planetary vehicles.

In a 1965 meeting at the Marshall Space Flight Center, its Director Dr. Werner Von Braun related his vision for lunar exploration to an incredulous Gemini IX trainee, Eugene Cernan. Cernan would later recall him casually remarking:

> “You will probably be driving a car on the moon” ([3, p 1])

Cernan’s scepticism may have had roots in the quality of his era’s auto mobiles. In 1965, Ralph Nader published “Unsafe at any speed: The Designed-In Dangers of the American Automobile”. It laid bare the wilful ignorance of automotive manufacturers to incorporate basic safety measures, even in the face of hard data. Nader cause célèbre, the American made Chevrolet Corvair.

Von Braun’s vision would come true and Cernan would become a strident advocate of its success.

> “It’s very tough on the surface. You can’t really judge inclines and distances and sizes very well, and the rover allowed us to cover this entire valley from both a scientific and a geologic point of view, bring hack samples and get pictures from places we never would have been able to get them from. We never would have been able to get to these places, I think that’s the most significant thing about the rover.”
>
> (Captain Eugene Cernan [3, p 205])

Cernan’s gratitude is not aimed at a single insightful engineer such as Thompson, but at hundreds working for NASA, Boeing and GM. Today, with a new NASA heavy launch vehicle within sight, armies of engineers are preparing for the second leap in manned rover design.

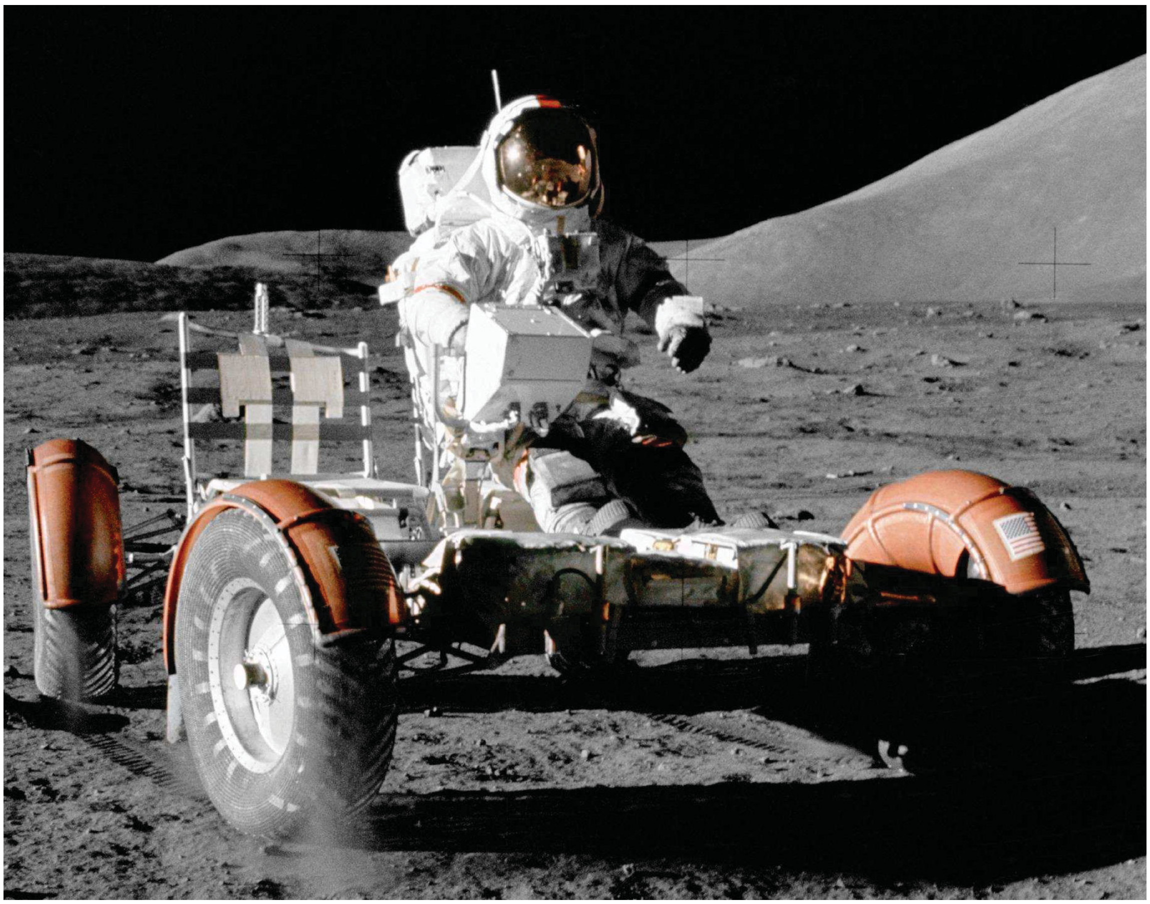

Figure 1–2: Apollo 17 astronaut Eugene Cernan driving the last Lunar Roving Vehicle (LRV) [4]

1.2 Rovers

The International Space Exploration Coordination Group (ISECG), of which the Canadian Space Agency (CSA) is a member, has begun researching hardware for Human Lunar Return (HLR) missions as a means of preparing for the human exploration of Mars [5].

Mueller estimates that the most ambitious possible HLR is four astronauts for 28 days. Initially, remotely operated vehicles would lay the groundwork for the mission by identifying landing sites and ice deposits for In Situ Resource Utilization (ISRU). Afterwards, a pair of pressurized rovers, capable of sheltering two astronauts each, would venture across the lunar highlands. The Design Reference Missions (DRM's) Mueller et al describe all take place at either of the lunar poles. Here, one can avoid the 15 day lunar night and the energy and thermal challenges this entails. However, the cratered polar highlands pose a more difficult ride comfort challenge for the rover suspension than was ever faced during the Apollo missions.

The CSA would appear to have adopted this position as it has both unmanned and human-rated rovers in various stages of design. The CSA's unmanned rovers are for NASA's Regolith and Environmental Science, and Oxygen & Lunar Volatile Extraction (RESOLVE) project [6]. In 2012, the third generation rover, Artemis Jr., completed a RESOLVE DRM in Hawaii [7] in preparation for a lunar mission slated to launch in 2017 [8].

Figure 1–3 shows simplified models of the CSA's second generation unmanned rover Juno II, and it's first generation human rated rover Artemis. Basic design parameters of Artemis, Juno II are compared against those of the the Apollo Lunar Rover (LRV) in Table 1–1 using specifications from NASA [9, 10], the CSA [11], the Lunar Sourcebook [12], Young's book "Lunar and Planetary Rovers" [13] and communications with Neptec Design Group [14].

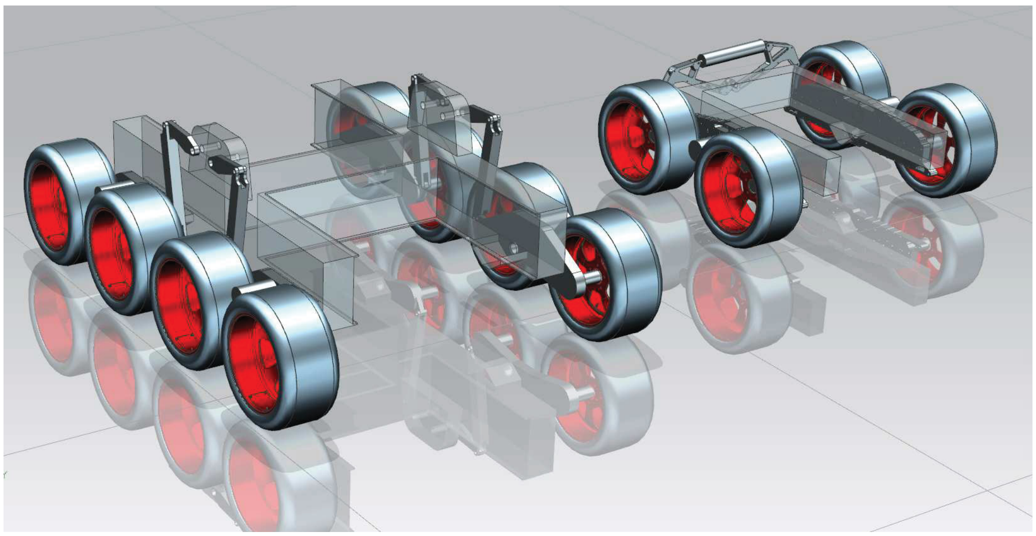

Figure 1–3: The CSA rovers Artemis (left) and JunoII (right)

Table 1–1: CSA rover specifications

		Juno I	Artemis	LRV
Operating environment		Lunar analogue sites		Lunar surface
Track Width	(m)	1.3	1.75	2.3
Wheel Base	(m)	0.8	2.25	3.1
Mass (No Crew/Cargo)	(kg)	180	500	218
Mass (Full Cargo-Crewed)	(kg)	365	800	708
Nominal Speed	(kph)	1	4.5	$6-7$
Top Speed (flat ground)	(kph)	5	15	13
Design distance	(km)	100's	100's	120

For Apollo, the astronaut mass is assumed to be 150 kg whereas for the CSA, the value is between 72 and 139 kg. In both cases, the crew make up the bulk of the cargo mass.

The CSA rovers Juno, Artemis and Artemis Jr all have wheels on the same side connected in pairs. Each pair is constrained by a pivot on the side of the vehicle. This resembles the tandem -axle suspension design used to facilitate trucks transporting heavy goods on rough terrain [2, 15]. Unlike trucks, wheels on opposing sides of the CSA rovers do not share a common axle. Instead, an independent drive-train in each bogie powers both wheels, allowing them to skid steer like a tank.

On Juno and Artemis Jr, bogies on either side are connected to each other by a differential beam which pivots about the rear of the chassis. This echoes the JPL rocker-bogie design found on its Mars Exploration Rovers, Spirit and Opportunity [16], as well as Carnegie Mellon's SCARAB rover [17]. The resulting suspension allows "body-averaging": the passive distribution of weight to all four wheels. Because it does so with rigid members instead of sprung ones, this suspension is purely kinematic in design.

The four bogies on Artemis are without the cross-chassis differential. Instead, each has its own torque arm which adjusts the balance in loading between the fore and aft wheel. Pre-load is adjusted by a torsional spring housed inside the chassis on the other end of each torque arm.

1.3 Wheels of the Apollo-Era

LRV's wheels have a minimum operating temperature of $-129\,°\mathrm{C}$, a temperature which is much colder than that of its fluid filled suspension dampers. Yet, due to thermal conduction from the lunar surface, it was the wheels which prevented the rover from operating in shadow for more than 30 minutes [9]. Compounding this thermal challenge is the wear caused by the moons abrasive lunar soil, or regolith, and the inertial loads when confronting the moons cratered surface.

A central tenet to NASA's design philosiphy is:

> "No single point failure shall abort the mission and no second failure shall endanger the crew" (Lunar and Planetary Rovers[3, p 16])

The pneumatic tire, which is a single puncture away from inoperability, is therefore not an option. Yet NASA did experiment with pneumatic tires on the Modularized Equipment Transport (MET) sent on Apollo 14. This hand-drawn "rickshaw" style cart could operate down to $-56\,^{\circ}\mathrm{C}$ thanks to a pair of synthetic tires and inner tubes [4]. Already on foot, immobilization was not the issue, it was the potential violence of a tire de-pressurizing [3]. Furthermore, the MET's tires (there was no suspension) could not provide enough compliance at its maximum speed of 4kph [10]:

> "[The MET] did bounce and hop and tipped to turn over if you hit rocks with the wheel or if you hit a crater with the wheel."
> (Edgar Mitchell [18, p 10-47])

This is why fifty years after its invention, the tire had to be re-invented in the 1960's to meet the requirements of the Apollo Lunar Roving Vehicle (LRV). This challenge spawned a slew of exotic ideas such as the conical shape of Grunman's wheel and the flexible sheet metal spokes of the Bendix wheel. Yet it was Goodyear's toroid of piano wire and titanium which demonstrated the best combination of handling, durability and ride according to a review of Apollo-era wheel designs by Asnani et al [10]. Ride appears to top the list for the mobility subsystem engineer for the LRV, Ferenc Pavlics.

> "We had to invent an all-metallic but still flexible wheel. Since this was a manned vehicle going at a reasonable speed over rugged terrain, it had to provide the astronauts with a good ride quality."
>
> (Ferenc Pavlics, [3, p 37])

Goodyear, in line with vehicle engineering tradition, didn't depart from present day bias-ply tires. They just removed the rubber.

(a) The Bendix wheel

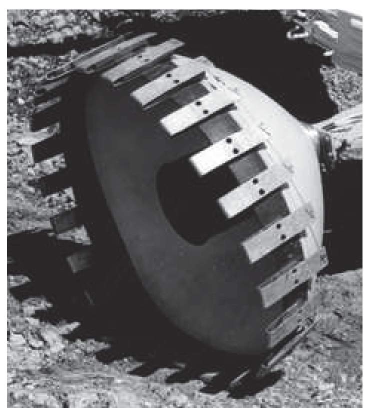

(b) The Grunman wheel

(c) The Apollo wheel

Figure 1–4: The first generation of lunar wheels made by Grunman, Bendix and Goodyear

1.4 Wheels Descended From the Apollo-Era

The second generation of lunar vehicles will face tougher terrain, polar highlands as opposed to equatorial mare, over distances ten times farther (100's of km), while supporting loads ten times heavier (100's of kg each). This new set of requirements is motivating a second re-invention of the airless wheel. Michelin is working on a more robust compliant spoked wheel, an iteration of the Bendix design. Goodyear meanwhile has opted to optimize the durability of the already proven Apollo wheel by replacing interwoven strands with interwoven coils. According to Goodyear's "Spring Tire" patent, this lessens fatigue while retaining a desirable balance between structural stiffness and local compliance [19].

Meanwhile, at McGill University in Canada, faculty engineers Peter Radziszewski and Sudarshan Martins drew a different conclusion from the Apollo wheel: If, like its predecessor the pneumatic tire we rely on fill for structure, could we remove all stiffness from the tire, and hence all sources of bending fatigue [20]? The answer is yes.

A carcass out of chainmail, "inflated" with a charge of 20,000 spherical particles [21] has exceeded the CSA's durability requirements by undergoing 200 km of field testing at 20 kph without sustaining *any* punctures large enough to allow particles to escape. This is ten times farther than required at 25% above Artemis' top speed. With its 4 mm ring chain-mail and 6 mm spherical particles, a puncture would be the result of several adjacent chain-mail links failing [22]. Based on the durability test, the probability of this occurring is small. In the event of a puncture, the loss of several particles per rotation allows the wheel to fail safely since the loss of all 20,000 particles would require many rotations of the wheel. Having proved its durability, the wheel is now dubbed iRings, short for iron rings, in reference to its carcass.

In this thesis, iRings is put to the test to see if it lives up to an even more ambitious goal envisioned by its inventors: To serve double duty as both wheel and shock absorber. The inspiration for this stems from Martins and Radziszewski's expertise in mineral processing.

Ore is often ground down by tumbling it onto itself in a horizontal drum. The faster the drum spins, the further the ore is pulled up the wall before it falls, and the further it falls, the more energy it dissipates like a wave crashing onto itself. Dissipation and speed are proportional up to the critical speed.

Davis defines the critical mill speed N_c as the point when equilibrium between centripetal and gravitational acceleration g is reached using only the mill diameter R to define the system.

$$N_{c,Davis} = \sqrt{\frac{g}{R}} \tag{1.4.1}$$

At this speed, dissipation and speed passively switch to an inversely proportional relationship. The faster the charge spins, the more it begins to behave like a rigid material: stiffer with less internal dissipation, or damping. Davis' definition, one of several, is the most useful for comparing iRings to a mill as it is independent of both mill operation and charge parameters.

Figure 1–5: The second generation of lunar wheels

(a) The Goodyear spring-wheel

(b) The iRings wheel

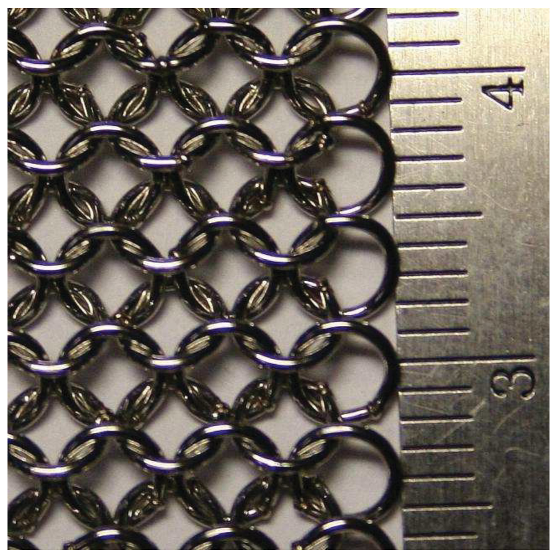

(c) The iRings chainmail tire

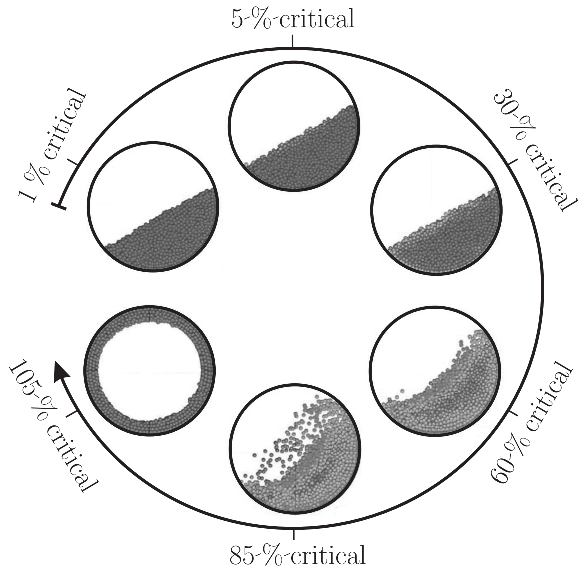

Figure 1–6: Charge motion versus speed of a horizontal grinding mill [23]

1.5 Thesis Objectives

Critical behaviour, which represents a limit to mill operating speeds, could serve as a means for a particle filled wheel to passively adapt its stiffness and damping to a vehicle's speed. The primary focus of this thesis is to determine what potential this has to enhance the comfort performance of the CSA's rovers.

To obtain these results with the available resources, the experiment is carried out in-silico with models of both wheels and rovers. Understanding the fidelity of this method compared to that of full vehicle field testing is the secondary goal this thesis aims to achieve.

1.5.1 Theoretical: Comfort Performance of iRings

The theoretical research question is broken down below into three secondary ones:

Q1-1 If particles are tumbled in a chain-mail cylinder as opposed to a rigid one, will they exhibit a critical speed? If so, how close is it to the speed predicted by the Davis equation.

Q1-2 If a critical speed is reached, will stiffness and damping change in a manner advantageous to ride?

Q1-3 Can the charge of iRings be used to adjust it's parameters enough to meet the ride requirements specified by the CSA?

1.5.2 Experimental: In-Silico Ride Test Fidelity

The virtual ride test takes place in a multi-body dynamics environment called ADAMS, which stands for Automatic Dynamic Analysis of Mechanical Systems. In it, the models in Figure 1–3 are excited by an individual linear actuator at each wheel moving with a frequency, phase offset, and magnitude designed to simulate driving on lunar terrain. By comparing the vehicle's frequency response to this excitation, an in-silico measure of ride performance is obtained. Unable to validate this test in-situ, the author instead questions the accuracy of the test's components by asking:

Q2-1 What is the fidelity of the iRings model?

Q2-2 What is the fidelity of the rover models?

Q2-3 What is the fidelity of the in-silico terrain inputs and ride measurements?

These questions can not be addressed until we meet the following objectives: (i) complete a review of the literature, (ii) define a testing methodology and then (iii) complete the experimentation. Each of the following three chapters will address one of these objectives which will be followed by a discussion addressing the questions posed. The work will close with a conclusion summing up the results and answers obtained.

CHAPTER 2
Literature Review

2.1 Introduction

In Section 1.5.1 of the introduction, the relationship between the angular velocity and ride performance of iRings is advanced as the focus of this thesis. Firstly, the literature review provides a primer in vehicle dynamics and granular dynamics in Sections 2.2 and 2.3 to explain ride in the context of a particulate filled wheel.

It then addresses the three secondary research questions regarding the relationship between critical speed, ride and percent granular fill of iRings in Section 2.4 by inferring lessons from the dynamics of the tumbling mill.

2.2 Vehicle Dynamics

Dixon frames both ride and handling in terms of passenger and tire "discomfort". It is a ratio of inertial forces caused by the movement across the terrain over gravitational forces due to mass [24].

$$\text{Passenger discomfort, } (D_P) = \frac{a_{z,rms}}{g} \tag{2.2.1}$$

$$\text{Tire discomfort, } (D_T) = \frac{\Delta F_{z,rms}}{F_{z,mean}} \tag{2.2.2}$$

where $a_{z,rms}$ is root mean squared (rms) vertical acceleration and $F_{z,rms}$ is rms vertical force.

The challenge in designing a lunar vehicle suspension is that decreased gravity amplifies the tire's sensitivity to discomfort while inertial effects remain the same. Bartlett's Vehicle Energetics (V.E.) ratio estimates tire discomfort by taking the ratio of a vehicle's forward momentum over its potential energy for the following scenario: A vehicle of mass m, designed to overcome obstacles of maximum height or depth h while travelling at speed v in a gravitational field g [17]. Mass cancels, giving:

$$V.E. = \frac{v^2}{2gh} \tag{2.2.3}$$

By this reasoning, a 1 inch high pebble on the moon might send a vehicle flying because its equivalent to hitting a 6 inch rock on earth. Worse still, discomfort increases quadratically with speed.

2.2.1 Ride

An equivalent theory to Bartlet's V.E. does not exist for ride; this is probably the reason the CSA adopts the ISO2631-1:1997 whole body vibration ride standard developed for passenger vehicles. In any case, a review of the effects of weightlessness in orbit finds that reduced gravity does not degrade sensitivity to linear acceleration [25]. This standard calculates a single ride value from the vehicle's frequency response in the following manner.

Begin by integrating the vertical acceleration response S_v over each one-third octave interval i of the frequency spectrum f between 1 and 80 Hz to obtain the one-third octave average acceleration a_i.

$$a_i = \int_{2^{i/3}}^{2^{(i+1)/3}} S_v(f)\,df \;,\; where\, i = 1\; to\, 19 \tag{2.2.4}$$

Following this, apply each octave weighting factor W_i to its corresponding acceleration a_i to obtain the weighted rms acceleration a_{wrms}.

$$a_{wrms} = [\sum_i (W_i a_i)^2]^{\frac{1}{2}} \tag{2.2.5}$$

The above equations is the ISO weighted rms acceleration value for comfort for a single direction and it ideally combines inputs from all three directions and all three moments. In this case, the CSA is only concerned with vertical, or "heave", accelerations likely because they provide an adequate estimate the main consequences of whole body vibration: Nausea, muskuloskeletal injury of the spine from chronic exposure and comfort [26]. This thesis considers only the former but as Section 2.2.3 shows, suspensions are designed with the latter two in mind.

2.2.2 The time domain

If possible, complex ride analyses are first simplified down to a Linear Single Degree of Freedom Model (LSDOF). The vehicle is reduced to a single wheel supporting a lumped mass m meant to represent its share of the vehicle's weight. Wheels become massless points of zero radius which follow the terrain like a needle on a record. Suspension linkages are replaced by a constraint allowing only vertical translation.

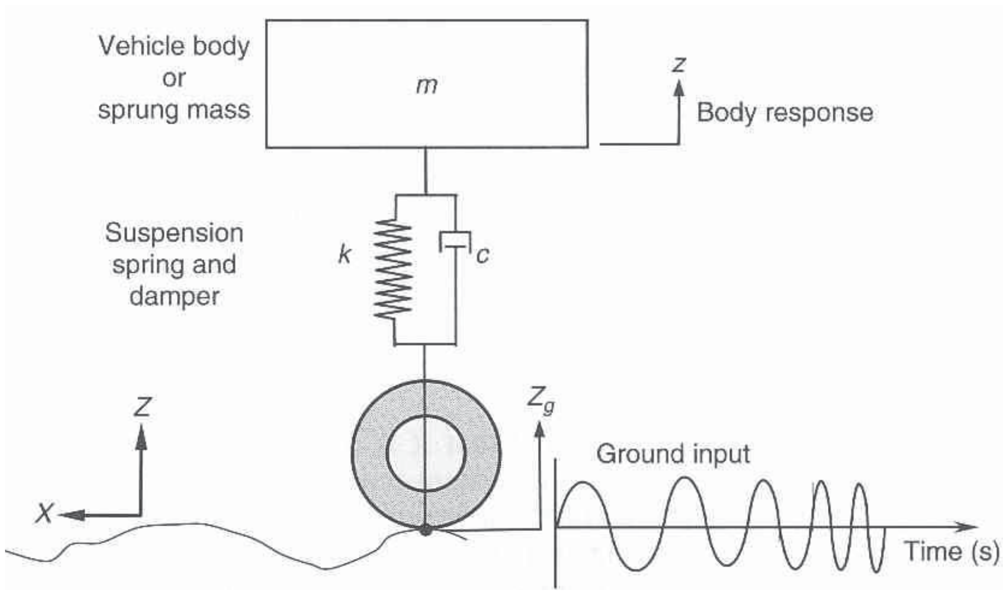

Figure 2–1: Linear Spring Damper Tire Model with point follower contact [27]

For vehicles without shock absorbers such as bicycles and tractors, the linear spring of stiffness k and linear damper of viscosity c are those of the tire. The terrain is represented as a rigid two dimensional ground elevation profile of height z_g. The result is the second order ordinary differential equation (ODE) below.

$$m\ddot{z} + c_{tire}\dot{z} + k_{tire}(z - z_g) = 0 \tag{2.2.6}$$

To represent a vehicle with shock absorbers, a second spring-damper pair can be added. This also requires separating m into the "sprung mass" m_s of the chassis above the shocks and the "un-sprung" mass m_u of the wheels and control arms below below them. This creates a model with two ODE's each representing tire and passenger discomfort respectively. In the next subsection, the frequency response of the two types of suspension are compared: those with shocks and tires, and those with only tires.

2.2.3 The frequency domain

In the figure below, Bartlett plots the response of a vehicle on a sinusoidal terrain similar to that on the right of Figure 2–1. The red line is the rms value of terrain height and the blue line is the rms value of vehicle displacement relative to it.

Note that the cut-off frequency for the shock absorber is a function of tire diameter and not suspension travel. The tire affords the suspension extra isolation by virtue of its shape and not its compliance, a property called "geometric filtering". This is perhaps the reason for the doubling in tire diameter between the MET and the LRV [12]. The bogies of Juno and Artemis also supply geometric filtering. Both effects are excluded from this analysis.

The wavelength in Figure 2–2 can be interpreted literally as obstacle length. However, terrain is more often represented as spatial frequency ω_s:

$$\omega_s\,(cycles/meter) = 1/(obstacle\,length) \tag{2.2.7}$$

Amplitude on the other hand is not interpreted literally as height but as energy - although it is the vehicle's momentum which introduces energy - obstacles merely convert it into vertical accelerations. To account for vehicle speed, assuming it is constant, spatial frequency is converted into a terrain's temporal frequency ω_t.

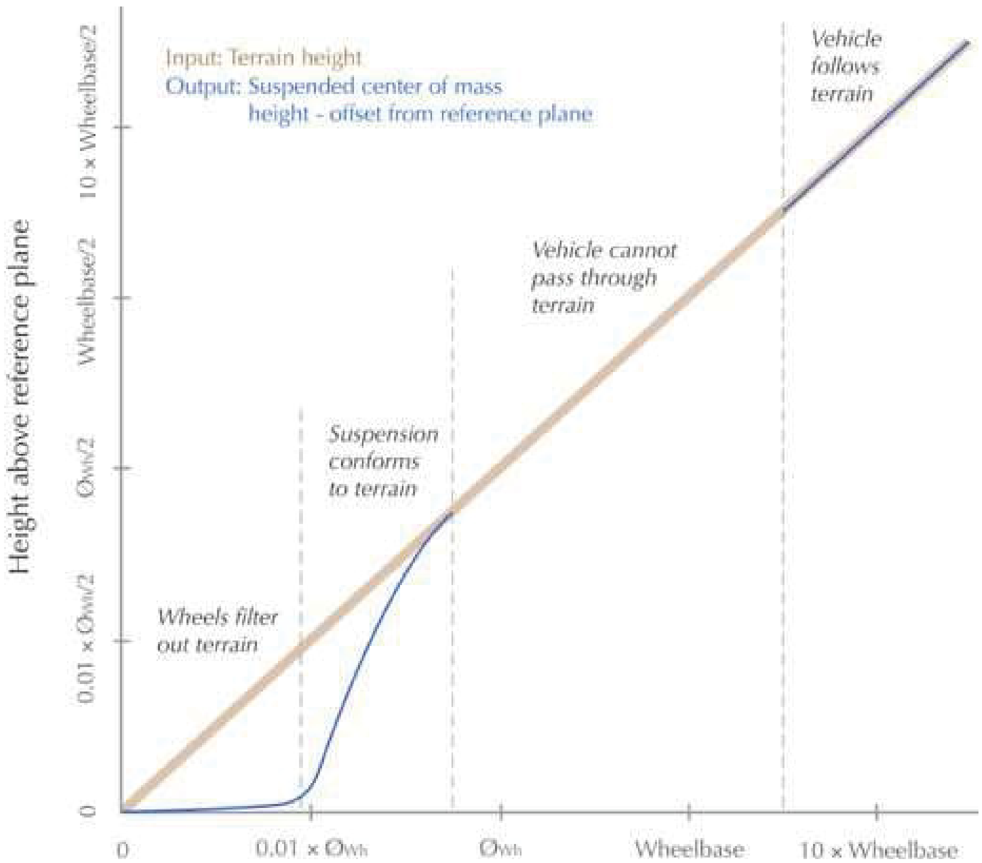

Figure 2–2: Vehicle heave versus terrain undulation measured relative to wheel diameter ($\oslash Wh$) and Wheelbase [17].

$$\omega_t(rad/s) = 2\pi \frac{speed(m/s)}{\omega_s(cycles/m)} \tag{2.2.8}$$

Bartlett sets the peak to peak amplitude of his sinusoidal terrain equal to wavelength. This amounts to assuming that terrain energy is proportional at all scales.

One often quantifies a suspension in terms of its gain (output over input). A transfer function characterizes displacement or acceleration gain. The plots of these gain functions are called transmissibility graphs. All three can be compared using the relationship below when the input is a sinusoidal terrain [28].

$$Power \propto (\ddot{z})^2 \propto ({\omega_t}^2 \cdot z^2) \tag{2.2.9}$$

Blundell [27] offers some fundamental insights into Equation 2.2.6 by deriving it's elevation (z) transfer function. The real component is:

$$|H(\omega_t)| = \frac{|z|}{|z_g|} = \sqrt{\frac{k^2 + c^2{\omega_t}^2}{(k - m{\omega_t}^2)^2 + c^2{\omega_t}^2}} \tag{2.2.10}$$

Plotting H against input frequency ω_t produces the frequency response graph in Figure 2–3.

Each supplemental spring-damper-mass adds another peak and the resulting transfer function is the dot products of their individual transfer functions. A detailed explanation can be found in either Genta or Wong [28, 29].

Note that ω_t is normalized by dividing it by the system's natural frequency ω_n:

$$\omega_n = \sqrt{\frac{k}{m}} \tag{2.2.11}$$

Stiffness and mass influence response shape by setting the location of resonance and the common inflection point $\sqrt{2}\,\omega_n$. As for transmissibility, it is determined by the damping ratio ζ.

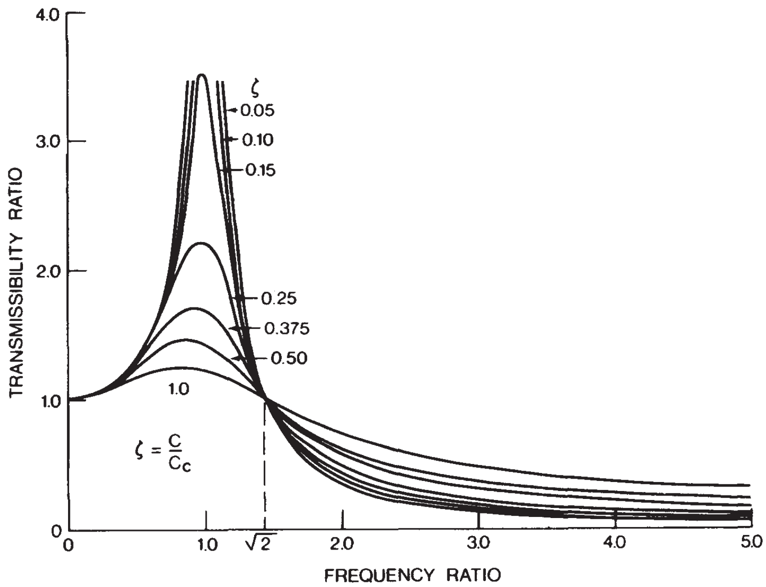

Figure 2–3: Transmissibility ratio of chassis displacement x over terrain obstacle size x_0 for a LSDOF system [29]

$$\zeta = \frac{c}{c_{critical}} = \frac{c}{2\sqrt{km}} \tag{2.2.12}$$

Using an two degree of freedom LSDOF model of a passenger car, Sugasawa et al find that a sprung mass with a damping ratio of 0.17 minimizes passenger discomfort while a ratio of 0.45 minimizes tire discomfort [30]. The unsprung mass for its part, will have a damping ratio 60% lower than its sprung counterpart[24]. For a single degree of freedom (SDOF), Genta arrives at a value of 0.354 [28].

Furthermore, the stiffness k should place the system's damped natural frequency ω_{nd} close to 1 Hz because this is the frequency which the human body tolerates best. The damped natural frequency ω_{nd} is defined as:

$$\omega_{nd} = \omega_n \sqrt{1 - \zeta^2} \tag{2.2.13}$$

Blundell suggests that this is a result of evolution as this frequency is also that of an adult's walking gait [27]. Recall that Eqs. (2.2.5) and (2.2.5) indicate that the lower the vehicle's mass, the faster it is moving, and the lower gravity is, the more important it becomes to keep resonance close to 1 Hz.

Conversely, the contents of the abdominal cavity resonate between 4 and 8 Hz, placing cyclic strain on the spinal cord and thereby making this range the most apt to cause chronic injury. To steer clear of this frequency band, the resonant frequency of passenger car tires is often in the 10-15 Hz range [31]. To achieve this, the unsprung mass is around five times less that of the sprung mass and the tire stiffness is ten times that of the shocks. Damping for its part is kept very low in tires in order to reduce rolling resistance losses. Kim et al find it to be around 1% in passenger vehicles [32].

Frequencies below 1Hz are uncomfortable as well as they affect the inner ear's vestibular system, resulting in nausea. In summary, for a tire to perform like a suspension in the frequency domain, damped natural frequency must decrease by an order of magnitude and damping ratio must increase from 1% to 30%. This is not as simple as it appears and the next subsection explains why.

2.2.4 A suspension with only tires

Equations (2.2.12) and (2.2.13) show that to achieve lower damped natural frequency and higher damping ratio, stiffness must decrease and damping increase. Genta offers a starting point, remarking that for solely optimizing ride in a SDOF model, k should be as low as the suspension travel will allow. As Equation 2.2.6 shows, a tire's travel has to increase in inverse proportion to the amount that stiffness is lessened. Unfortunately, with increased travel comes increased variation in the tire's torque arm and thus increased tire discomfort

When wheel travel can no longer be increased, a decrease in the damping coefficient is the only remaining recourse for attaining the desired resonance and damping factor. One has little choice in fact because otherwise the tire's resonance if left with low damping can cause it to lose contact entirely, an effect known as "wheel hop". This places a limit on the speed of tractors for certain terrains [31, 33].

The Apollo and Spring wheel manage to filter terrain energy without either decreasing contact stiffness, increasing contact damping nor increasing travel by using envelopment [10, 19]. Their carcass behaves like a collection of springs. Like a mattress, their collective stiffness supports the load while each individually conforms to local point loads. This strategy is nonetheless limited to obstacles which are an order of magnitude smaller than the contact patch length and vertical compliance.

The particles in the iRings wheel allow envelopment [22] but the rolling drop test is not designed to measure it. What the test does measure is the wheels potential to passively adapt it's stiffness, damping and side-wall height with speed to sufficiently store and dissipate the increase in energy input. The relationship between these design parameters and speed is the topic of the following subsection.

2.2.5 Adaptive suspension

Uys and Thoresson simulate an off-road vehicle with a semi-active air-ride suspension travelling between 10 and 50 km/h on terrains such as pasture and ploughed land. Their results show that damping should increase with rising roughness and decrease with rising speed while stiffness should increase for both. Note that stiffness is raised mainly to control not the damping ratio, but the suspension travel, which is maintained constant throughout [34]. One can therefore also conclude that travel should increase in proportion to speed and roughness as well. They also find that optimizing ride on a specific road type at various speeds will also optimize ride on other terrains.

Most suspension components derive their properties from the manipulation of oil, air, rubber or metal. With some simplification, their values can be assumed to be constant and to influence both speed and displacement linearly. Tuning a suspension which relies on granular media is a whole different affair as the next section explains.

2.3 Granular dynamics

When poured from the confines of a container, a granular material flows like a liquid; when it meets a flat surface, it regains the ability to support shear like a solid, forming a pile [35]. Hence the name of an emerging continuum mechanical theory of granular materials: Granular Solid Hydrodynamics (GSH).

2.3.1 Granular elasticity and damping

A 90% filled iRings wheel contains 20,000 half inch diameter polypropylene spheres. Together, they exhibit a bulk stiffness less than that of polypropylene and a bulk material damping coefficient which is greater. This section uses the three types of energy transformation which underpin GSH to explain this behaviour.

A dry granular material can transmit forces solely through compressive particle to particle interactions resembling those in Figure 2–4b. Idealizing the particle geometry as spherical, Hertz's contact equation defines the contact force F_c as

$$F_c = k\delta^{3/2} \tag{2.3.1}$$

where δ is the local deformation at the contact zone and k is the material's elemental stiffness. What makes spherical geometry distinct is that contact pressure is initiated over a vanishingly small area, magnifying the contact force and allowing compression, albeit minute, which other geometry would have made impossible. The exponent of 3/2 represents the non-linear relationship between indentation and contact area which makes further deformation require more and more force.

At the meso-scale, Figure 2–4a, these interactions take on the form of the force chains. Particle chains are analogous to springs in series and thus reduce the bulk stiffness of the material [35].

Off-road vehicles often have to deal with compliance in the granular materials they are driving on using the theory of terramechanics. For instance, using Bekker's pressure-sinkage equations Park et al calculate that dry LETE sand could exhibit a stiffness of 32 kN/m. This is non negligible since tires are often in the 100's of kN/m.

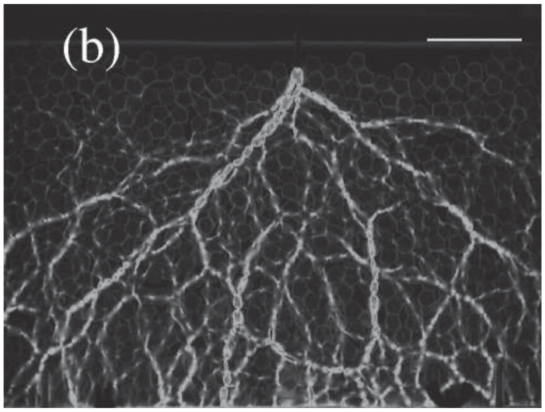

(a) Meso-scale force chains [36]

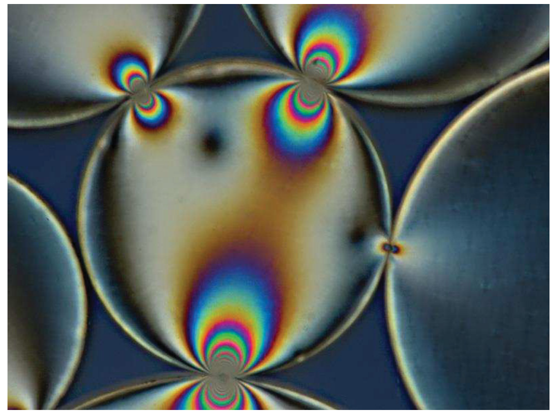

(b) Particle-scale force chains [37]

Figure 2–4: Force chains, resulting from a static point load, made visible using the photoelasticity technique with perspex discs.

NASA models both terrain stiffness and damping for its rovers using a software called ROAMS, an acronym for Rover Modelling and Simulation [38]. It determines the contact force using the Hunt and Crossley equation

$$F_c = k\delta^n + c\delta^p\dot{\delta}^q \tag{2.3.2}$$

Here, n allows stiffness to vary with any geometry while p and q permit damping to vary non-linearly with speed and a separate non-linear indentation-contact area relation [39].

2.3.2 Confining pressure and Reynolds Dilatancy

Hunt and Crossley's coupling of damping to compression makes sense for iRings. The force chains in iRings will be constantly rearranging themselves as the wheel turns. The rolling and sliding of particles necessary for this to happen allows energy to escape the system thermally [35]. As compression z increases, packing density can increase by up to 20% [40]. This is called a “jammed” state because reduces the degrees of freedom of the particles. Jammed granules, with little room to roll and slide, offer less damping.

As external forces increase, force chains consolidate and eventually form shear bands along which clumps of “jammed” particles can slip. Once completely consolidated, jammed clumps are like a car jammed in traffic: its motion requires the neighbouring particles to move as well. This effect, called Reynolds Dilatancy , is the reason a consolidated granular material swells when it is forced to shear [41, 42].

Sometimes, boundary conditions can allow pressure to increase without the material failing. In this case, jammed particles begin to transmit elastic waves in the manner of a continuum solid. In essence, it stiffens. The next section explains how jamming occurs in a tumbling mill and what it could mean for the stiffness and damping of iRings.

2.4 Granular flow and Tumbling Mills

The more a granular material shears, the more its internal energy becomes kinetic. In this regime, damping is a function of the randomness of particle motion, in other words entropy. This state is called granular flow and this thesis approaches it not with GSH, but instead with the semi-empirical equations developed to characterize a similar system: the tumbling mill. The granular flows of a tumbling mill and of iRings have two forces in common: gravitational and centripetal. While gravitational force remains constant, centripetal force grows with speed.

2.4.1 Critical speed

Davis, along with Rose and Sullivan, Watanabe and Hertz offer critical speed relationships based on geometric and dynamic properties of the mill and charge. Davis is useful for comparing iRings to tumbling mills because it requires only that they both be cylinders with a fixed radius R. It does so by assuming negligible particle radius r relative to R ($r << R$), an internal coulomb shear angle Θ_c of 90 deg and by neglecting slip between the charge and the mill.

Yet even this single assumption is flawed. The limp chainmail carcass is unable to prevent the radial pressure of the centrifuging particles from expanding its diameter and shrinking its width. Although theoretical estimates of diameter versus speed at varying gravities are offered in the iRings patent, this metric is outside the scope of this thesis [21]. Nonetheless, the relationship with iRings' diameter, and concordantly its travel, has with speed is an advantageous one according to Uys et al. Reducing contact width, and thereby area, also improves rolling resistance.

Martins introduces a new aspect of critical speed called "critical behaviour" which attributes to this transitional state discontinuities in measurements of entropy, mean energy and energy [23]. If jamming affects both these properties as well as stiffness and damping, it follows that discontinuities in the latter should be observed as well. If damping and stiffness vary the same way in iRings as in a mill, then this would be advantageous for ride on both counts according to Section 2.2.5.

2.4.2 The effect of percent fill in tumbling mills

Percent fill is the fraction of the volume, including voids, which the particles occupy inside a tumbling will. For iRings, the 100% reference fill is determined experimentally by filling iRings as much as the chain-mail and rim can allow. The present design allows a maximum of 21,053 half inch diameter polypropylene particles.

A dimensional analysis by Rose and Sullivan predicts that at sub-critical speeds, the power P required to rotate a mill (or in other words, its damping) and the percent fill α of a mill are inversely proportional [23].

$$\frac{P}{D^5 N^3 \alpha} \propto 1 + \frac{0.4\sigma}{\alpha} \tag{2.4.1}$$

Where D represents mill diameter, N is rotational speed in radians per second and σ is the energy variance of the fill.

Watanabe defines the relationship between critical speed and percent fill as

$$N_{c,Watanabe} = \sqrt{\frac{g}{R\, sin\Theta_c \sqrt{1-\alpha}}} \tag{2.4.2}$$

where Θ_c is the Coulomb friction angle of the charge and R is the mill's internal radius. By this relation, decreasing iRings' percent fill from 90% to 80% while keeping its diameter and charge the same should result in a 15% decrease in critical speed.

2.5 Conclusions

Regarding the main research focus of this thesis, iRings may display elasticity if loads are compressive and it can also dissipate energy thermally or kinetically depending if the fill is jammed or unjammed respectively. The literature review also provides hypotheses for the three secondary questions. First, confining pressure could both increase its stiffness and reduce its damping albeit non-linearly in both cases. Second, centripetal forces in a spinning wheel increase confining pressure and modify stiffness and damping in a manner advantageous for ride. Third, percent fill may provide adjustability of both damping and the critical speed. In summary, iRings has the potential to serve as a passively adaptive suspension component.

Pneumatic tires also change their compliance and dissipation with speed in the 0-20 kph range due to the viscoelasticity of their carcass [29]. Only a few facilities around the world posses machines designed to apply loads to rotating tires [43]. These are also instrumented to churn out parameters for semi-empirical equations developed specifically for pneumatic tires. The following chapter explains how both of these challenges were surmounted using the resources available to the author at McGill University.

CHAPTER 3
Research Methods and Materials

3.1 Introduction

The secondary focus of this thesis is to qualitatively assess the fidelity of the in-silico ride test performed on the CSA rovers, Juno and Artemis, while equipped with iRings wheels. Lacking the ability to validate this data with in-situ testing, this chapter examines how the author manages to simulate the main components of the test. Section 3.2 deals with the creation of the iRings model and Section 3.3 addresses how it is validated. Section 3.4 discusses the vehicle models as well as the basis for the inputs and the measurement of outputs from the in-silico ride test.

3.2 Wheel data acquisition and model development

The design of the iRings tire model is a two step process. First, its transient response to an impulse is measured at varying angular velocities using a custom built "rolling drop-test". Second, an LSDOF model is fitted to the response in Matlab using a Parameter Identification Algorithm (PIA) written by the author. Matlab is a high-level language and interactive environment for numerical computation, visualization, and programming.

3.2.1 The rolling drop test

A drop test, such as the one described by Wong [29], is capable of determining the vertical response of a wheel across its entire frequency spectrum by applying an impulse and measuring the transient acceleration decay [44]. Because the iRings wheel is capable of changing its properties with angular velocity, a constant speed must also be delivered. This hybrid solution is dubbed a Rolling Drop Test (RDT).

The rear suspension and drive-train of the McGill Baja vehicle in Figure 3–2a provides the necessary control of the wheel's angular and vertical motion. The position of these two motions are captured respectively by a proximity sensor and accelerometer, shown mounted to the suspensions in Figure 3–2b. The sensors outputs are recorded at 500 Hz by a Compact Reconfigurable Input Output (c-RIO) data acquisition module made by National Instruments and customized for this application. Detailed information on the test hardware is available in Appendix A.

Here is a summary of how to use the Rolling Drop Test. First, hoist a wheel 6 inches from the ground using a rope and pulley and secure in place with a pin. If the engine is running, allow the wheel to reach a steady speed before releasing the pin. Secondly, once the wheel has made contact with the High Density Polyethylene (HDPE) "landing pad", allow its vertical oscillations to decay completely before stopping the engine.

Perform thirty independent runs for each combination of fill (80 or 90%) and speed (0, 44, 87, and 131 rpm). Assuming the test will yield at least 25 error-free runs, this ensures a five-fold decrease in the average standard deviation σ by the following relation.

$$\sigma_{average} = \frac{\sigma_{run}}{\sqrt{no.\ of\ runs}} \tag{3.2.1}$$

Figure 3–2: Two views of the rolling drop-test

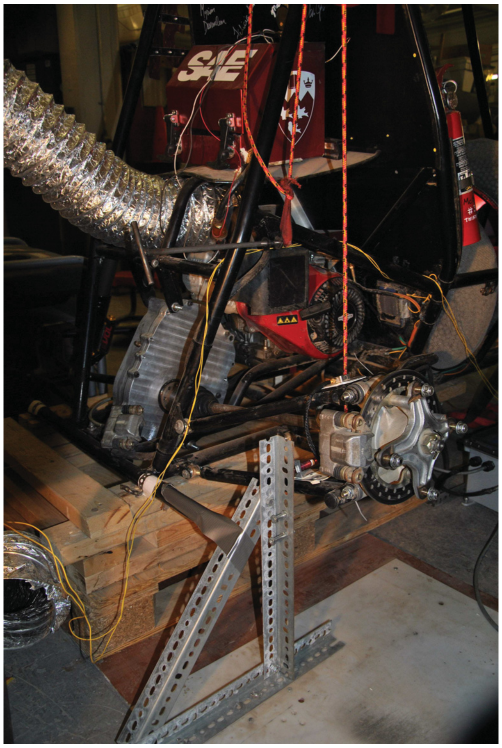

(a) The McGill Baja rear suspension and drivetrain, modified and instrumented

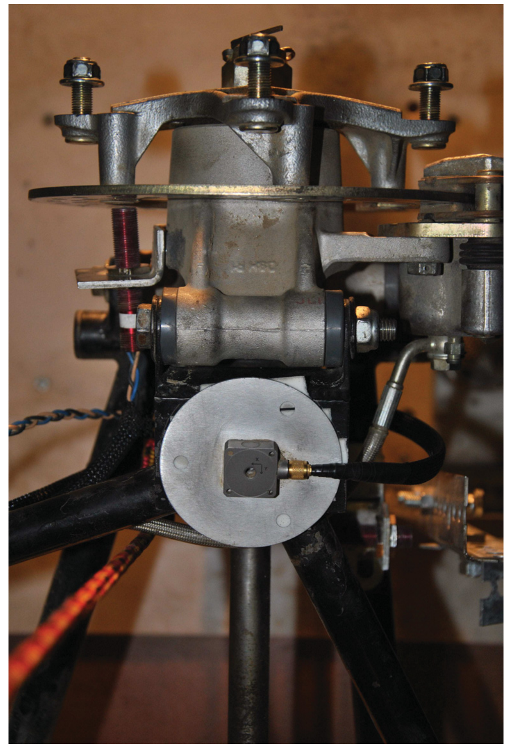

(b) Top view: The three axis accelerometer taped to the top control arm and the wheel speed sensor mounted to the wheel hub

3.2.2 The parameter identification algorithm

Solving the ODE in Equation 2.2.6 with respect to vertical acceleration yields

$$z(\ddot{t}) = Ae^{-\zeta\omega_n} cos(\omega_{nd} \cdot t) \tag{3.2.2}$$

First, the Parameter Identification Algorithm (PIA) smooths out the engine noise in the resulting $z(\ddot{t})$ using a Butterworth low-pass filter. The filter is designed to eliminate the engine frequencies which begin at 33 Hz (44 rpm) while leaving signals below 25 Hz, where the bulk of wheel's harmonics reside, unaffected.

Second, the PIA extracts the decay envelope from the filtered $z\ddot{(t)}_{filtered}$ using the Hilbert Transform (HT). For a detailed description of how this function works, consult Feldman [45].

Third, the tPIA fits the exponential function

$$\ddot{z}(t)_{filtered} = Ae^{(-\alpha \cdot t)} \tag{3.2.3}$$

to the decay envelope using the non-linear least squares tool in Matlab.

Fourth, by assuming the frequency response is linear, the PIA can substitute the frequency of the highest peak for ω_{nd}. The damping ratio ζ and the natural frequency ω_n are then derived using Equation 2.2.13 and the relationship

$$\alpha = \zeta \cdot \omega_n \tag{3.2.4}$$

Following this, the values c and k are found, using Eqs. 2.2.11 to 2.2.13, in order to construct the LSDOF model in Equation 2.2.6. Because the LSDOF does not vary with wheel speed, the PIA must be repeated for each data set. The next subsection describes how this result is validated with a virtual Rolling Drop Test.

3.3 Validation of the RDT and the ADAMs wheel model

The results of the RDT are verified for accuracy and systematic error.

Systematic error, is measured by studying the probability distribution of the ζ values derived from the response data of each run. With data sets close to 30, the distribution is expected to be Gaussian if no other processes or errors are present [46].

Accuracy is measured by performing 0 rpm tests on an OEM pneumatic tire. Frequency and time domain responses are compared to those of a linear system while stiffness and damping coefficients, whose derivations are explained in the following section and compared to the results to independently measured data. The AT-489 is selected as the control since it matches the dimensions of iRings, but it must be compared to other OEM tires as Carlisle does not make data on the AT-489 available. Also, errors introduced by the rotation cannot be verified as a rotating pneumatic tire would generate too much friction with the HDPE "landing pad".

Table 3–1 compares the properties of iRings wheel to a pneumatic benchmark, the AT-489, and a non-pneumatic benchmark, the Apollo wheel.

Table 3–1: At-489, iRings and Apollo tire specifications

		Carlisle AT-489 model 589329	iRings 80-90% fill	Apollo Wheel
Diameter	(in)	23.1	22-24	32
Width (ground)	(in)	7.4	10-11	9
Mass (with rim)	(kg)	8.42	32.9-34.6	5.5
Maximum static load	(kg)	127	N/A	61
Carcass material		Bias 3-ply Rubber	4 mm Stainless Chain-mail	Piano wire Titanium Chevrons
Fill		Air, 7 psi	17-19 k Polypropylene Spheres (0.5" Dia.)	Titanium Hoops

3.3.1 The ADAMs wheel model

This test reproduces the RDT in ADAMs to determine the fidelity of the LSDOF when implemented in this environment. Figure 3–3 shows the rigid bodies whose shape and mass approximate those found in the RDT. The 20,000 particles, the chainmail and rim of iRings are all modelled as rigid bodies symmetric about the wheel axis and the vertical plane. Not shown is the “SFORCE” connecting the center of the tire to a point projected vertically onto the ground. This is a force based on the LSDOF model, which calculates the instantaneous value of vertical contact force by using measurements of the velocity and position of the center of mass of the wheel. The appropriate c and k parameters are input at each speed although the only moving parts are the suspension linkages. The ideal frictionless joints placed at their rod ends and journal bearings are hidden as well. For a more detailed description, see Appendix B.

The validation makes direct and indirect comparisons; frequency spectra will be compared graphically, while average values of ζ derived from both spectra are plotted against speed. The implementation of the LSDOF in ADAMs is expected to generate slightly different results for the following reasons:

First, as iRings intersects the ground plane, the velocity goes from zero to a non-zero value instantaneously [47]. To avoid generating an infinite SFORCE, an ”S” shaped step function gently transitions its values through 0 to 0.01 mm of deflection.

Secondly, as the wheel begins to separate from the ground, it experiences a tensile damping force as the indentation velocity is now negative. Although this

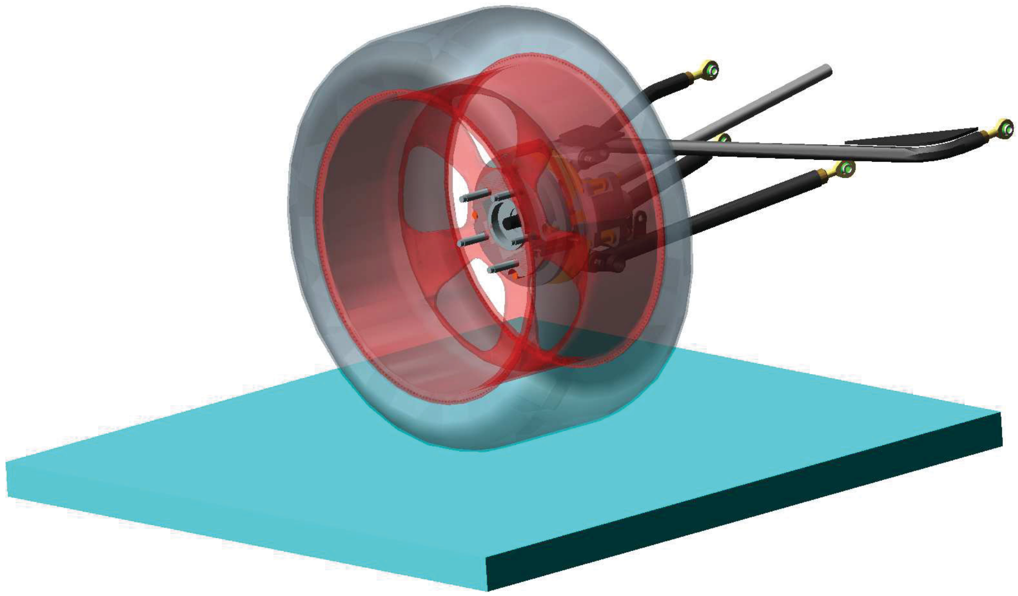

Figure 3–3: ADAMs wheel drop test setup

is faithful to the model, it clearly is unphysical as granular solids cannot transmit tensile loads.

Thirdly, when deflection falls below zero, the SFORCE turns off allowing gravity alone to determine position.

3.4 The ADAMs Multi-Post ride test

The full vehicle ride test performed in ADAMs is based on the in-situ four-post actuator test used to simulate roads inputs in the laboratory. The rovers are matched to models of the iRings wheel and the whole is placed on a set of virtual linear actuators. A constraint applied at the geometric center of the rover restricts horizontal translation to prevent the vehicle from slipping off its posts.

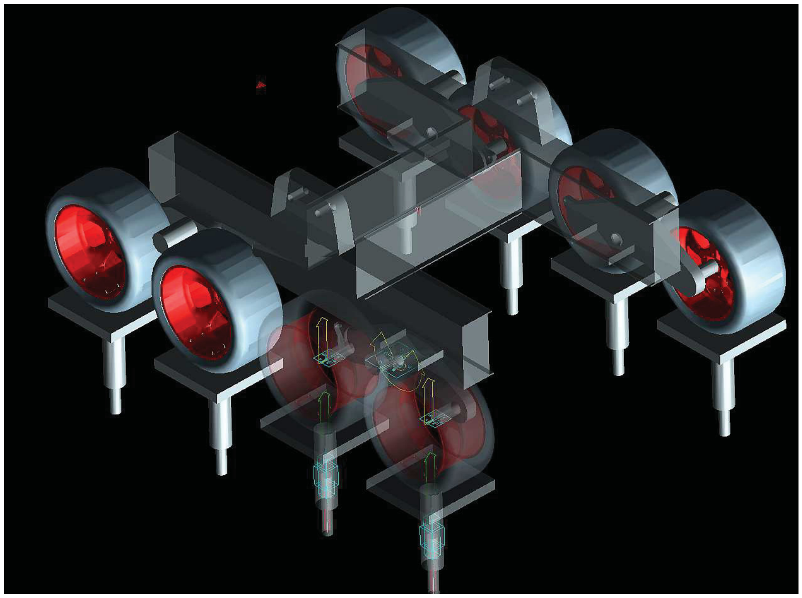

Figure 3–4: The Artemis rover on the eightpost setup in ADAMS

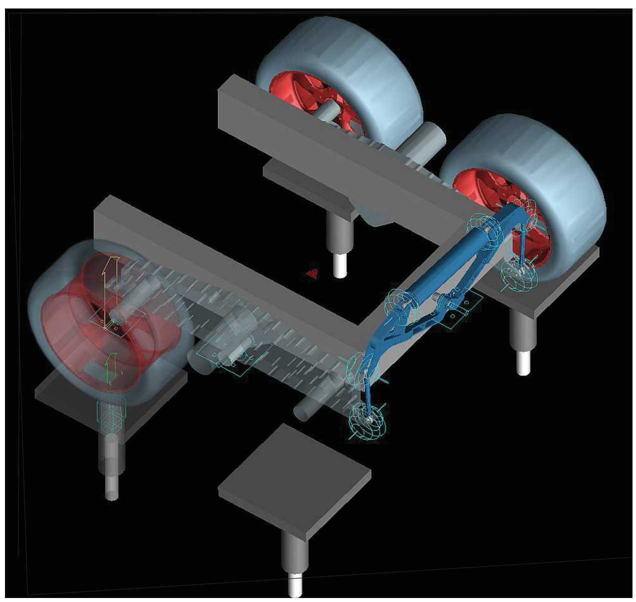

Figure 3–5: The Juno rover on the fourpost setup in ADAMS. One wheel is hidden for clarity.

The Multi-Post test has several advantages over the quarter car test shown in Figure 2–1. Firstly, by combining four or eight LSDOF tire models with the rover's suspension, it can output moments in three dimensions as opposed to just one. For now however, ride measurements are taken at the center of mass of the vehicle and these moments are ignored since the CSA does not specify a driver position on the rover.

Secondly, a point follower normally struggles to remain in contact at temporal terrain frequencies above 2.5 Hz [48] due to its lack of envelopment compliance and geometric filtering. By applying only vertical forces, a wider range of terrain frequencies can be tested although it ignores the compliance available on the iRings wheel.

3.4.1 Rover output: Measuring Ride

The CSA specifies a passenger threshold weighted rms acceleration of 2.5 m/s^2, which appears very conservative when compared to the ISO comfort scale in Table 3–2. What the ISO values fail to account for is the isolation provided by the seat. This difference could prove considerable if the CSA opts for an advanced air ride seat as its counterpart NASA is now considering [49]. Generalizing the requirement to a broader class of vehicles, Table 3–3 lists the CSA's vibration limits for non-human rover payloads such as communications, power and vision systems [50].

Figure 3–6 places these requirements in context by comparing them to three curves showing the threshold at which human proficiency is diminished [51]. At

Table 3–2: ISO comfort scale[26]

	rms weighted acceleration	
	g's ($a_{rms}/9.81$) unit-less	a_{rms} m/s^2
perception limit	0.0015	0.015
not uncomfortable	< 0.032	< 0.315
a little uncomfortable	$0.032 - 0.064$	$0.315 - 0.63$
fairly uncomfortable	$0.051 - 0.9812$	$0.5 - 1$
uncomfortable	$0.82 - 0.163$	$0.8 - 1.6$
very uncomfortable	$0.127 - 0.255$	$1.25 - 2.5$
extremely uncomfortable	> 0.204	> 2
CSA human exposure limit	0.255	2.5

Table 3–3: CSA rover to payload PSD limits [50]

Frequency range Hz	Maximum permitted vibration environment on Rover -Allowable chassis vibration- $(m/s^2)^2/Hz$	Vibration Environment for Payload Design -Payload exposure limit- $(m/s^2)^2/Hz$
$0.0 - 0.1$	$96.2E + 01$	$1.92E + 02$
$0.1 - 2.0$	$96.2E + 01$	$1.92E + 02$
$2.0 - 2.5$	$8.97E + 01$	$1.79E + 02$
$2.5 - 500$	$2.54E - 01$	$5.07E - 01$

low frequencies, human occupants dictate vibration isolation requirements, while at higher frequencies it's the rover payload's turn.

3.4.2 Actuator Inputs: Simulating terrain

The assumption made by Blundell in Figure 2–2 is that terrain energy is proportional to spatial frequency at all scales; this is a gross simplification. In reality, terrain energy drops off sharply with scale [24]. Sayers et al demonstrate how the Discrete Fourier Transform (DFT) can be used to demonstrate this. When applied to a random terrain profile such as the one on the left of Figure 2–1, the DFT assigns a discrete power value to each terrain wavelength ω_s throughout the spectrum of interest [52]. Naturally, the plot is called a Power Spectral Density

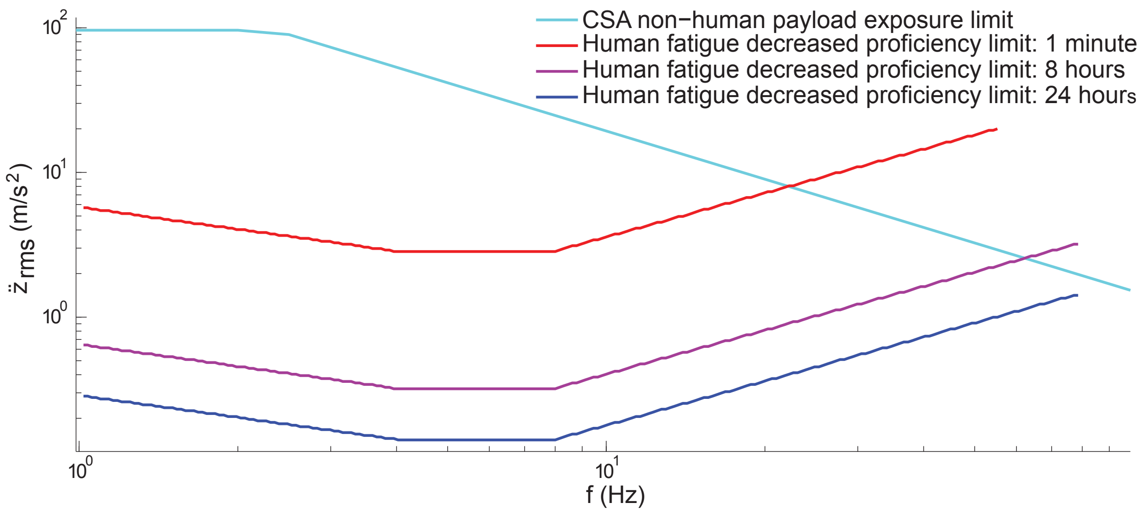

Figure 3–6: RMS acceleration curves of constant comfort for equipment [50] and human occupants based on exposure [51].

(PSD) of terrain elevation. It can be simplified further by fitting it with the exponential equation [53]

$$PSD = C(\omega_s)^{-N} \tag{3.4.1}$$

where C (cycles/meter) is a measure of a terrain's absolute roughness and the exponent N is a measure of much its roughness varies with spatial frequency ω_s. The CSA, and hence this study, adopts the ISO standard 8606:1995 which finds a value of $N = 2$ representative for most terrains relevant to passenger vehicles [28].

In Table 3–4, the CSA specifies two terrains for the Artemis rover whose absolute roughness C differs by 7%. For each terrain, the CSA specifies the combination of speed and load the Artemis rover must be able to handle while not exceeding the human and hardware vibration exposure limits given in Table 3–3.

This thesis uses the same terrains for the Juno rover but imposes a speed of 2.5 kph and a total mass of 180 Kg to reflect the nature of its unmanned prospecting mission [54]. Juno for its part, need only respect the hardware exposure limits specified in Table 3–3.

Table 3–4: Artemis test conditions defined by the CSA[50]

	Surface condition	Surface roughness constant 'C' $m^2/(cycles/m)$	Surface roughness constant 'N'	Load Kg		Speed kph	
				Artemis	Juno	Artemis	Juno
max load	surface 1	$1.92E+02$	2.00	800	180	4.50	2.5
min load	surface 1	$1.92E+02$	2.00	500	180	4.50	2.5
max load	surface 2	$1.79E+02$	2.00	800	180	10.50	2.5
min load	surface 2	$1.79E+02$	2.00	500	180	10.50	2.5

Figure 3–7 puts the CSA terrains, as given in Table 3–4, in context by comparing them to the Lunar mare [12] and to off-road Terrestrial terrains [29].

3.5 Conclusions

This methodology examines the assumptions inherent in the four main building blocks of the ADAMs ride test. The least well characterized is the iRings wheel prototype and consequently it is subject to three forms of validation. One, by testing the Carlisle AT-489 pneumatic tire alongside iRings, its response and LSDOF model parameters can be compared to independent values of similar tires, assessing the accuracy of the drop test. Two, by attempting to reproduce the RDT in-silico with a model of iRings, artefacts introduced by ADAMs or the Matlab algorithm are ferreted out. Three, by examining the probability distribution of damping ratios obtained from individual drop test runs, the independence of the tests measurements is evaluated.

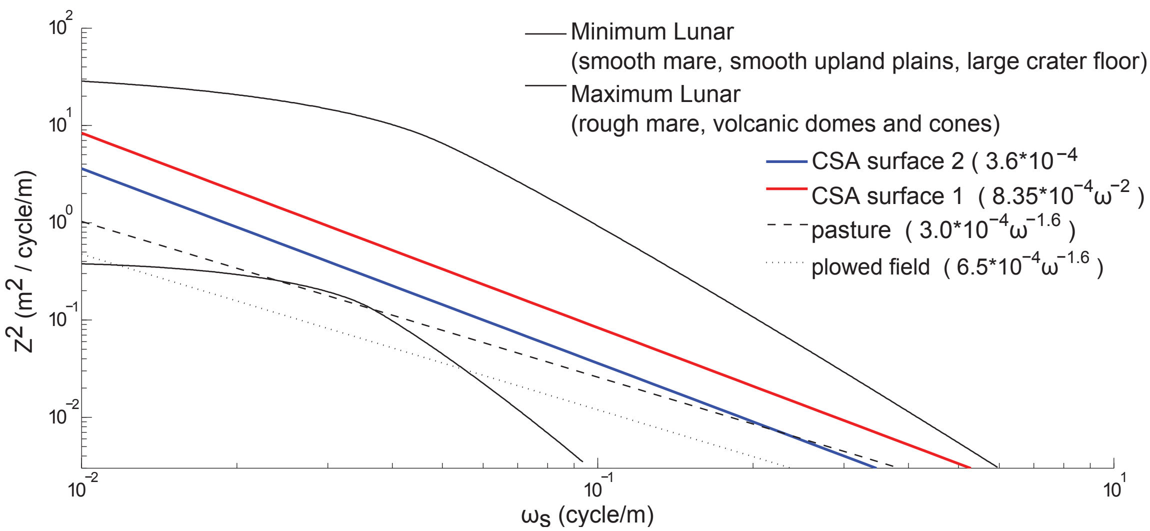

Figure 3–7: A comparison of Lunar, Terrestrial and the CSA's terrain PSD's [12, 29, 11]

The three remaining building blocks are the rover models, terrain inputs and ride measurement methodology. These are supplied to the author by the Neptec design group, the CSA and ISO 2631 ride standard respectively - only the manner in which they are implemented in the test is assessed here.

In summary, the main source of error in the ride test is iRings; the most significant assumption about its behaviour is that its bulk properties are linear in the 0-25 Hz band. The wheel and rover test results in the following chapters provide some answers.

CHAPTER 4
Results

4.1 Introduction

In this chapter, wheel test results are combined and compared to facilitate answering the ride performance and methodology performance questions posed in Chapter 1. First, Section 4.2 links the behaviour of iRings' fill to its natural frequency. Next, Section 4.3 highlight trends between iRings' operating parameters and its tire dynamics parameters. Following this, Section 4.4 contrasts the linear frequency response of the AT-489 with that of the iRings wheel. Section 4.5 then compares their time domain responses.

Afterwards, Section 4.6 validates the ADAMs model by comparing its in-silico frequency responses to the in-situ ones in Section 4.4. Then Section 4.7 compares the stiffness and damping of both wheels to each other and benchmarks them against the Apollo and Goodyear designs. Following this, Section 4.8 examines critical speed and its relationship with fill and provides additional validation of ADAMs data. Finally, Section 4.9 reports the results from the ADAMs Multi-Post ride tests.

4.2 Visual Data

During the wheel testing campaign, images are captured from video footage shot at 60 frames per second. Figure 4–1a, shot $2/60^{ths}$ of a second after impact, shows particles falling on either side of the rim create two lumps. A blue dot and a green line added to the footage reveal that the wheel is oscillating at 4 Hz with a peak to peak amplitude of 1 inch. This is the same frequency as the largest peak in Figure 4–2.

Figure 4–1: Video frames of the 80% filled iRings wheel throughout a 131 rpm drop test. Sub-captions indicate the time, post-impact, in seconds.

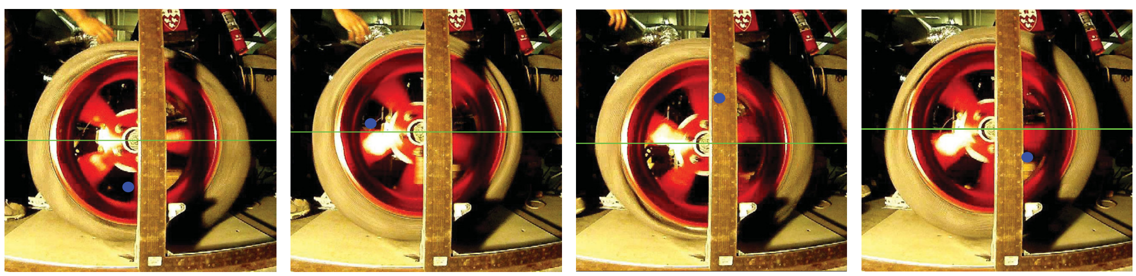

(a) $2/60^{ths}$ (b) $9/60^{ths}$ (c) $17/60^{ths}$ (d) $25/60^{ths}$

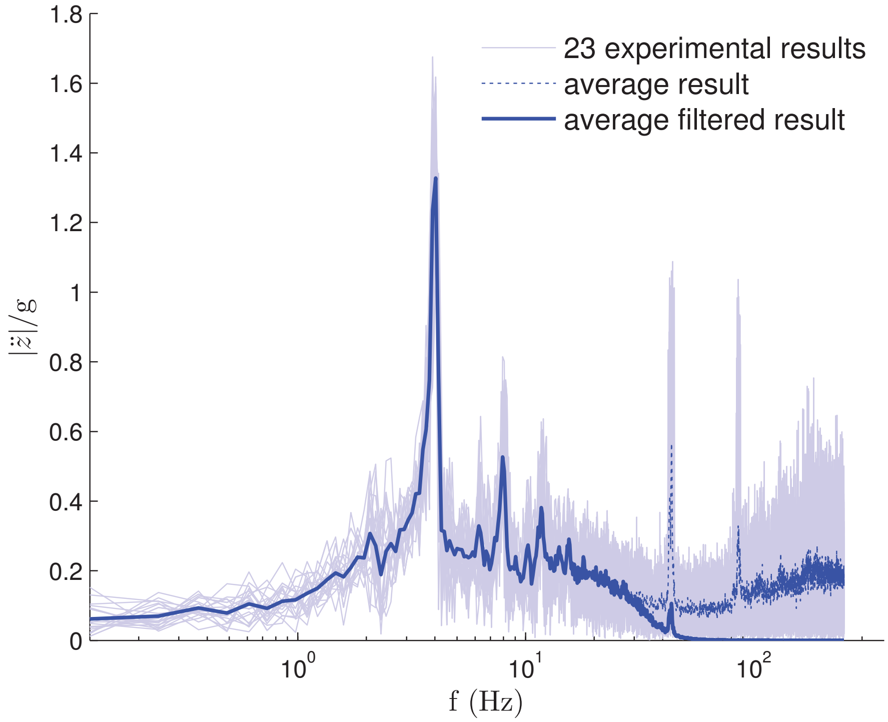

Figure 4–2: Frequency response for iRings at 80% fill, 131 rpm.

4.3 Comparison of 80% and 90% Filled iRings Wheels

In Figure 4–4, progressively sharper peaks from 0 to 131 rpm point to a trend of decreasing damping with speed for both fills. Arranged by speed in Figure 4–3, the frequency responses are very similar for both fills. The same can be said for the time domain responses. This is why the analysis will focus on the 90% fill results with the 80% fill results presented in detail in Appendix B.

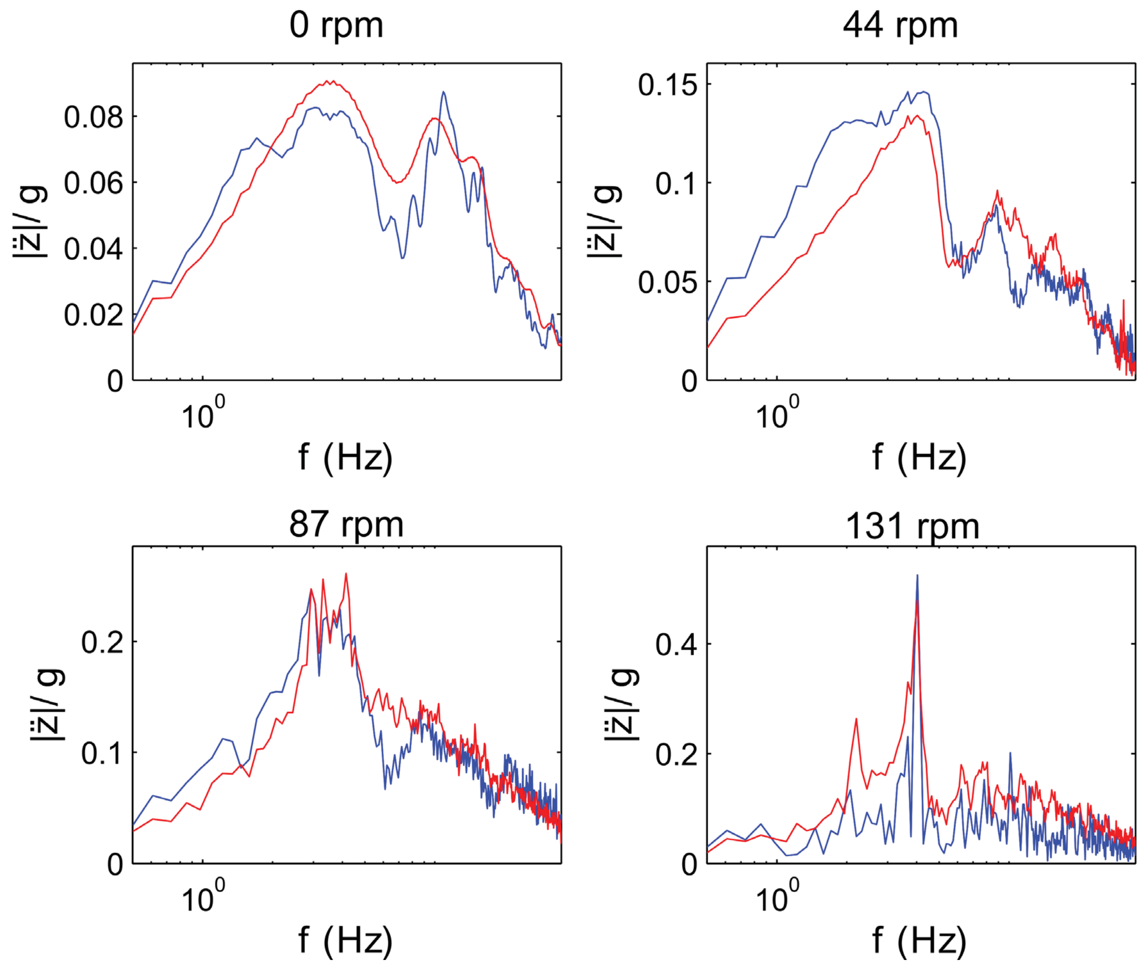

Figure 4–3: Comparison of 0, 44, 87 and 131 rpm iRings Frequency Responses at 80% and 90% Fill

Figure 4–4: Comparison of 90 % Filled iRings Frequency Responses at 0, 44, 87, and 133 rpm

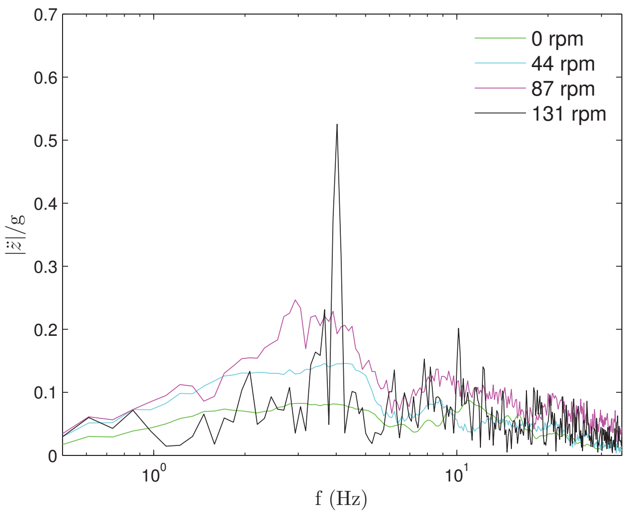

(a) 80% Filled iRings Wheel

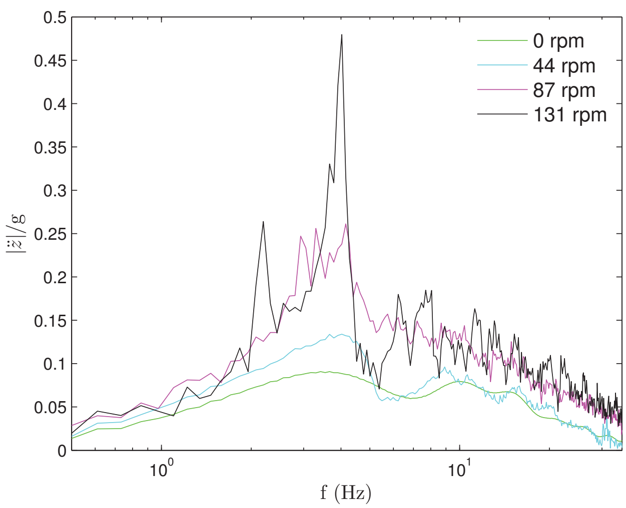

(b) 90% Filled iRings Wheel

4.4 Frequency Responses: The AT-489 and 90% Filled iRings Wheel

In this section, individual responses are the pale lines, the dotted line is their average and the solid line is the filtered average. The filter, a low-pass Butterworth, is necessary because averaging alone cannot remove the the two engine harmonics near 35 and 70 Hz in Figs. 4–6b to 4–6d. For consistency, the filter is applied to non-rolling drop test data as well. From here on, frequency responses refer to the filtered results only. Note that individual responses which deviate sharply from the average were assumed to be outliers and removed.

Figure 4–5: AT-489 Frequency Domain Response to Rolling Drop Test

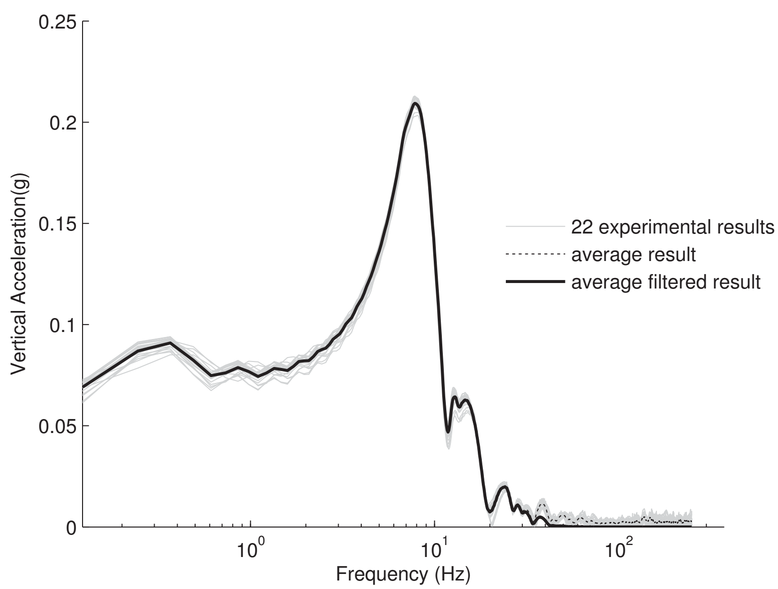

Comparing Figs. 4–5 and 4–6, it is apparent that the AT-489 comes much closer to having the single peak characteristic a linear system than does iRings.

Figure 4–6: 90% Filled iRings Time Domain Response to 0, 44, 87 and 131 rpm Rolling Drop Test

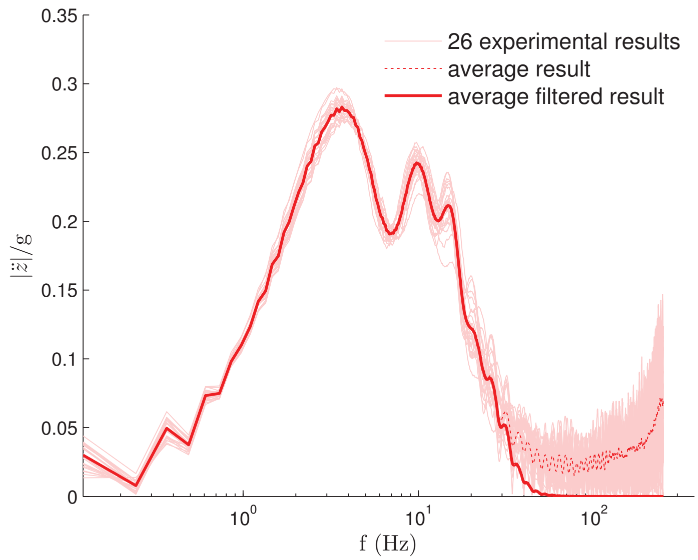

(a) 0 rpm

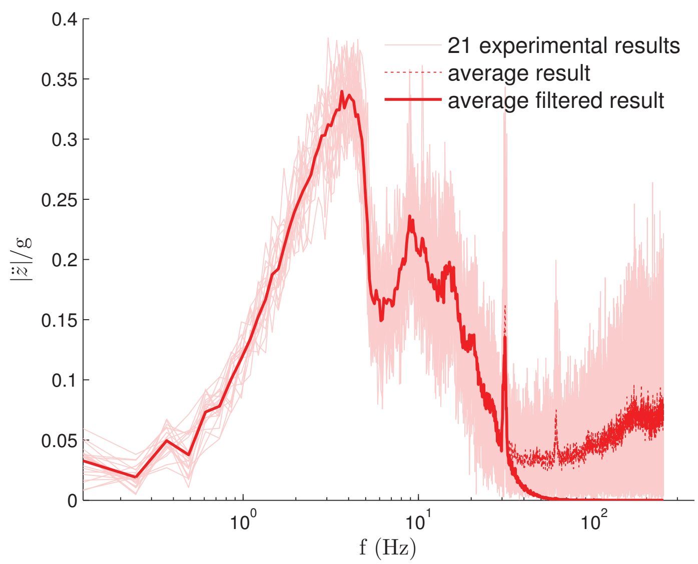

(b) 44 rpm

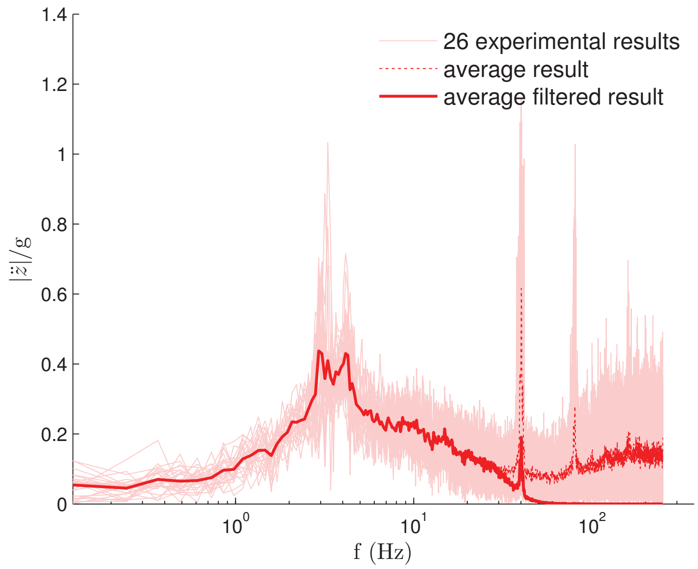

(c) 87 rpm

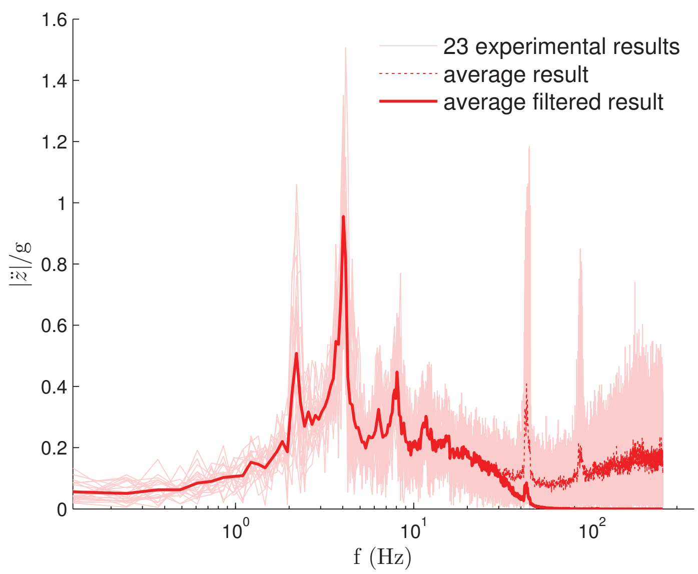

(d) 131 rpm

4.5 Comparison of the LSDOF Model and Rolling Drop Test

In this section, individual responses are the pale lines, the dotted line is their average and the solid line is the LSDOF model response. The model response is an average as well having been built using the mean stiffness and damping values derived from each individual response. Note that individual responses which deviate sharply from the average were assumed to be outliers and removed.

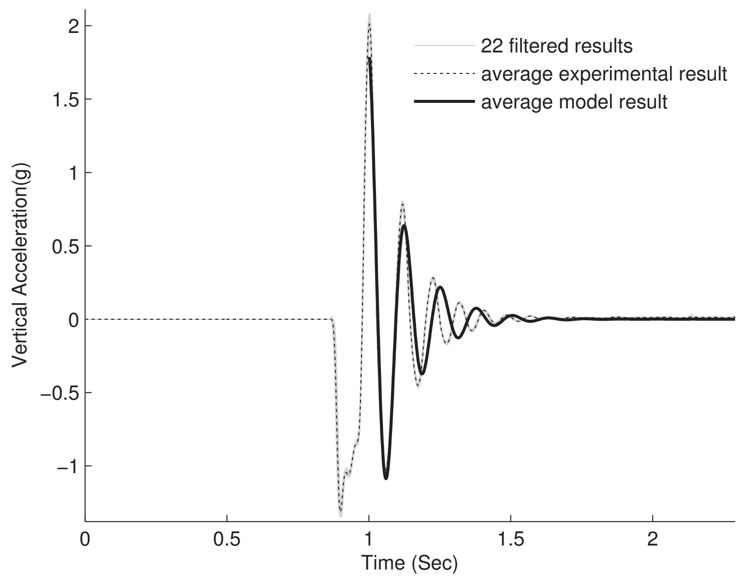

Figure 4–6: Comparison of AT-489 Time Domain Response to 0 rpm Rolling Drop Test and Quarter Car Model

The time domain response of the AT-489 is easily matched by the LSDOF model in Figure 4–6 while it struggles with the iRings time domain responses in the following figures.

Figure 4–7: 90% Filled iRings Time Domain Response for 0, 44, 87 and 131 rpm Rolling Drop Test and LSDOF Model

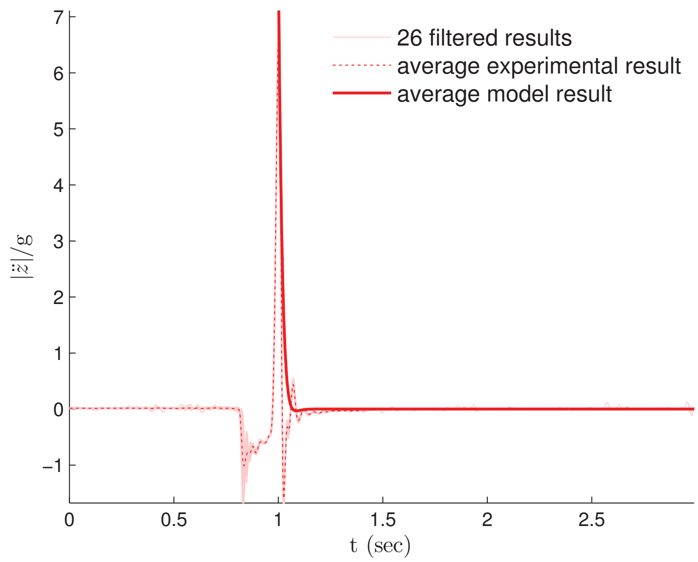

(a) 0 rpm

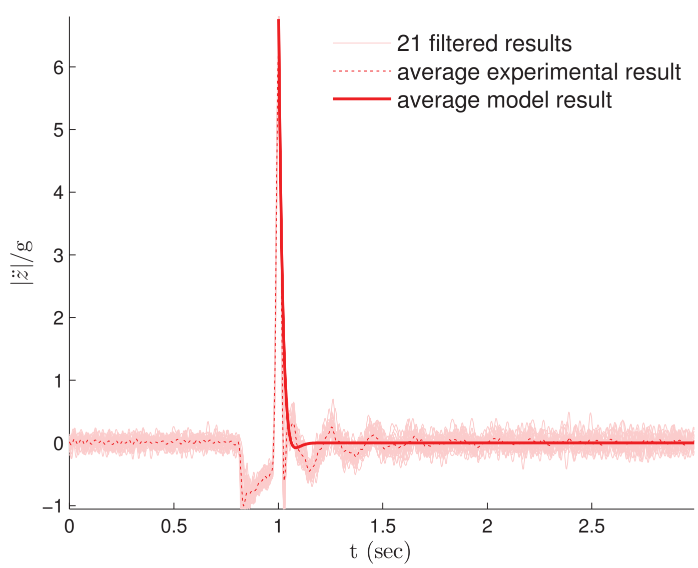

(b) 44 rpm

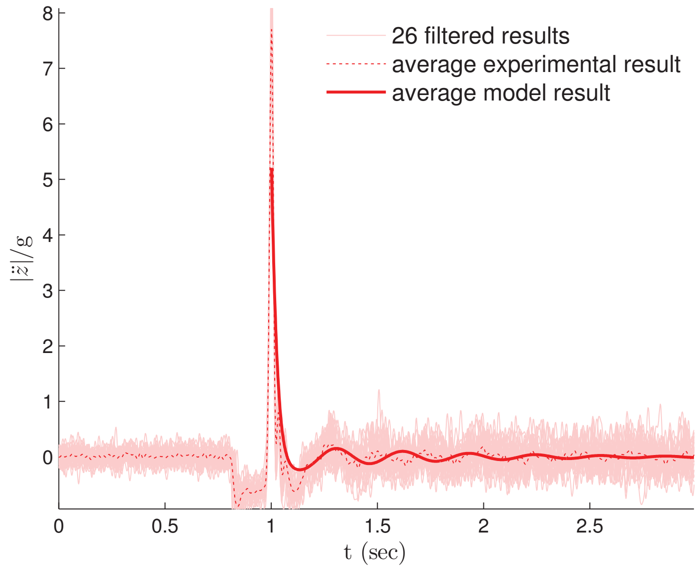

(c) 87 rpm

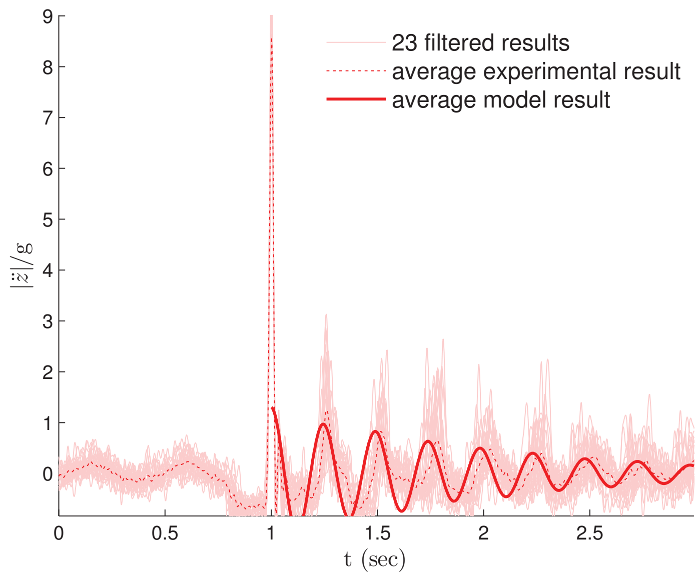

(d) 131 rpm

At 0 and 44 rpm, the model matches the first peak but not the subsequent oscillations; at 131 rpm its the opposite case; at 87 rpm it matches both.

4.6 Comparison of In Situ and In-Silico Drop Tests

The figures below compares the frequency response of the in-situ rolling drop test (a red line) and the in-silico ADAMs drop tests (shaded foreground). Figures are cropped at 20 Hz as this is near where the ADAMs model begins to diverge.

Figure 4–8: Comparison of 90% Filled iRings Frequency Domain Response to 0,44, 87 and 131 rpm In-Situ and In-Silico Rolling Drop Tests

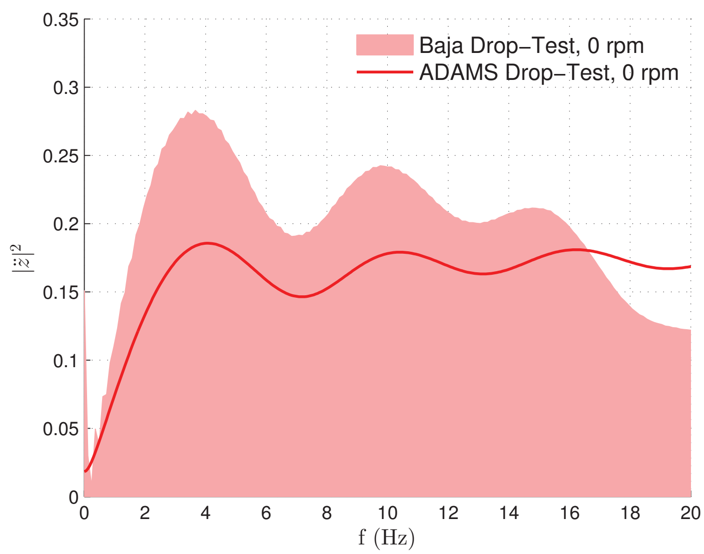

(a) 0 rpm Response

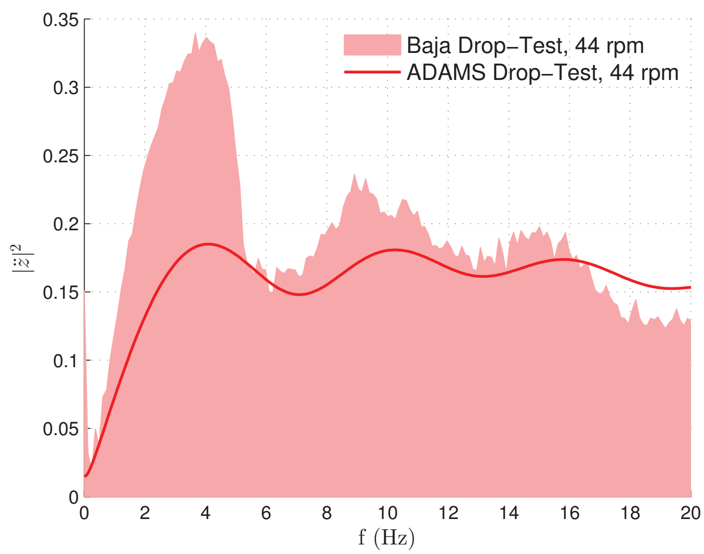

(b) 44 rpm Response

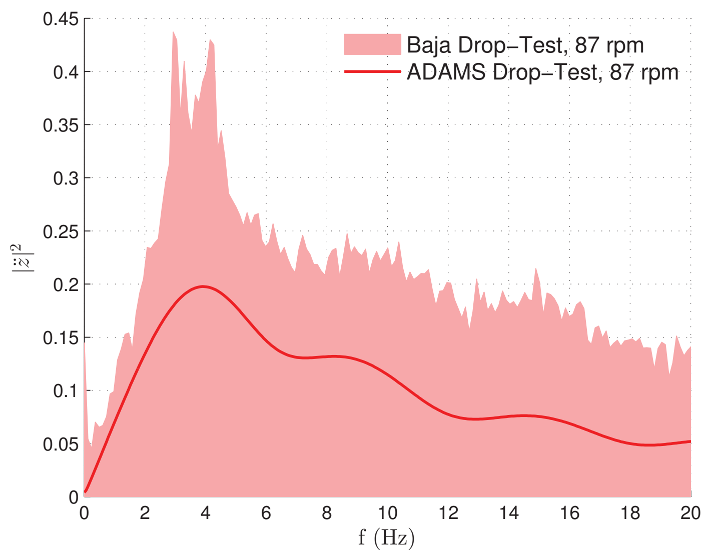

(c) 87 rpm Response

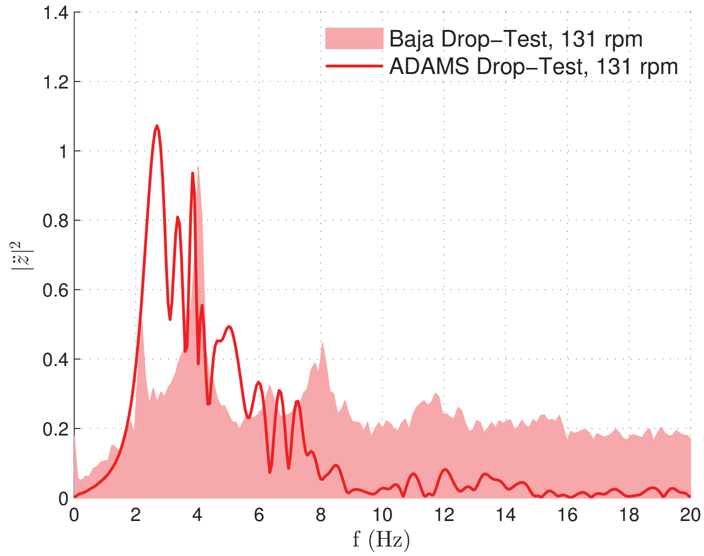

(a) 131 rpm Response

4.7 Stiffness and Damping Parameters

The LSDOF system identification algorithm derives damping and stiffness parameters from the in-situ and in-silico drop tests in the same manner. The only difference is the ADAMs data was not averaged nor filtered. The parameters of the AT-489 and iRings are compared to each other in Table 4–1 and to pneumatic and non-pneumatic wheels in Table 4–2 and Figure 4–7. The AT-489 clearly resembles the car tire most, while iRings falls less neatly into a single category. Going by stiffness, iRings resembles a tractor tire at 0 to 44 rpm and a car tire at 87 and 131 rpm.

In Figure 4–7, the stiffness of iRings resembles that of the Goodyear Spring Wheel while at 0 and 44 rpm and that of the LRV wheel at 87 and 131 rpm.

Note that the bi-linear LRV stiffness represents its softer piano wire mesh on the outside and its stiffer titanium bump stops on the inside. The piano wire mesh

Table 4–1: Wheel model parameters

	Mass (Kg)	Angular Velocity (rpm)	Stiffness k (kN/m)	Damping c ($kN \cdot s/m$)	Damping Ratio ζ	Damped Natural Frequency ω_d (hz)
iRings 80% filled	32.88	0	691.5	9.0	0.92	3.64
		44	222.3	4.6	0.88	3.87
		87	109.0	3.1	0.66	3.26
		131	21.70	0.046	0.034	3.99
iRings 90% filled	34.55	0	762.2	9.4	0.92	3.63
		44	415.6	6.6	0.84	4.04
		87	42.09	1.5	0.80	3.34
		131	21.72	0.060	0.027	3.99
Pneumatic Tire (7 Psi)	8.42	0	47.98	7.9	0.1669	0.315

is described as an "under-inflated tire" by Ferenc Pavlics [3]. The Goodyear wheel for its part, is described as being suitable for off-road and mining vehicles [55] which makes it comparable to a tractor tire. Recognize that the Goodyear Spring Wheel stiffness in this graph is that of the terrestrial prototype whose springs are encased in polyurethane. In its patent, Goodyear describes the wheel as being less stiff without the polyurethane but does not specify to what degree. As for damping coefficients and ratios, no values have been found by the author for either wheel.

Table 4–2: OEM Pneumatic Tire Specification

	Dynamic Stiffness k (kN/m) Non-Rolling	Dynamic Stiffness k (kN/m) Rolling	Inflation Pressure (psi)	Damping Coefficient c ($kN \cdot s/m$)	Damping Ratio ζ
Truck Tires	N/A	764 - 1024	N/A	N/A	N/A
Tractor Tires	219 - 438	300 - 700	10 - 30	0.36 - 3.4	N/A
Car Tires	N/A	125 - 275	15 - 35	2.86 - 4.89	0.027 - 0.095

Values in the table above are from Wong [29] and Kim et al. [32].

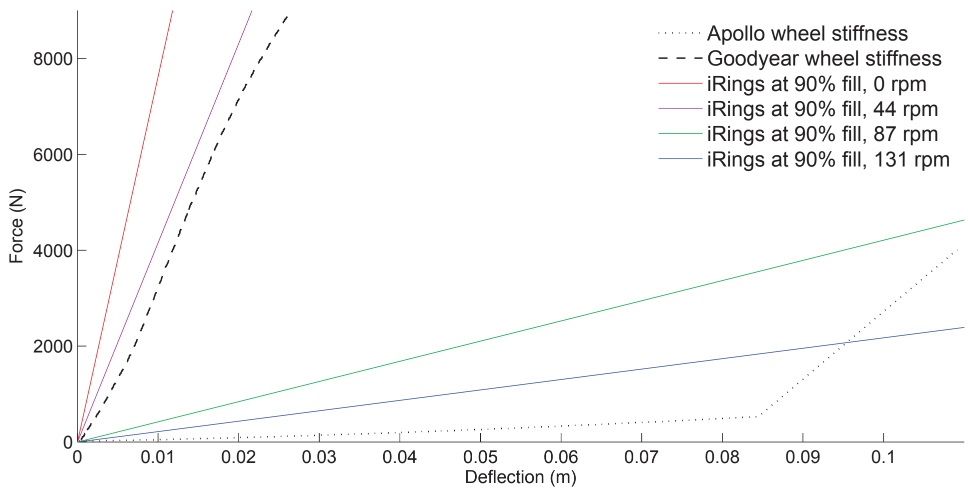

Figure 4–7: Stiffness of Apollo, Goodyear and iRings

4.8 Damping Ratios

Figure 4–9 contains damping ratios derived from in-silico and in situ drop test data. Confidence intervals of two standard deviations on the experimental data show that the ADAMs data is reliable except at 44 rpm. A Piecewise Cubic Hermite Interpolating Polynomial (PCHIP) fit using Matlab shows two things. First, sharp bends in the in-situ polynomials hint at a critical transition between 44 and 87 rpm. Second, an offset to the right of the 80% in-situ polynomial suggests a proportional relationship between fill and critical speed.

Probability distributions of individual experimental damping ratios in Figure 4–10 are Gaussian at 0 and 131 rpm and non-Gaussian at speeds in between. This affirms the presence of a critical transition.

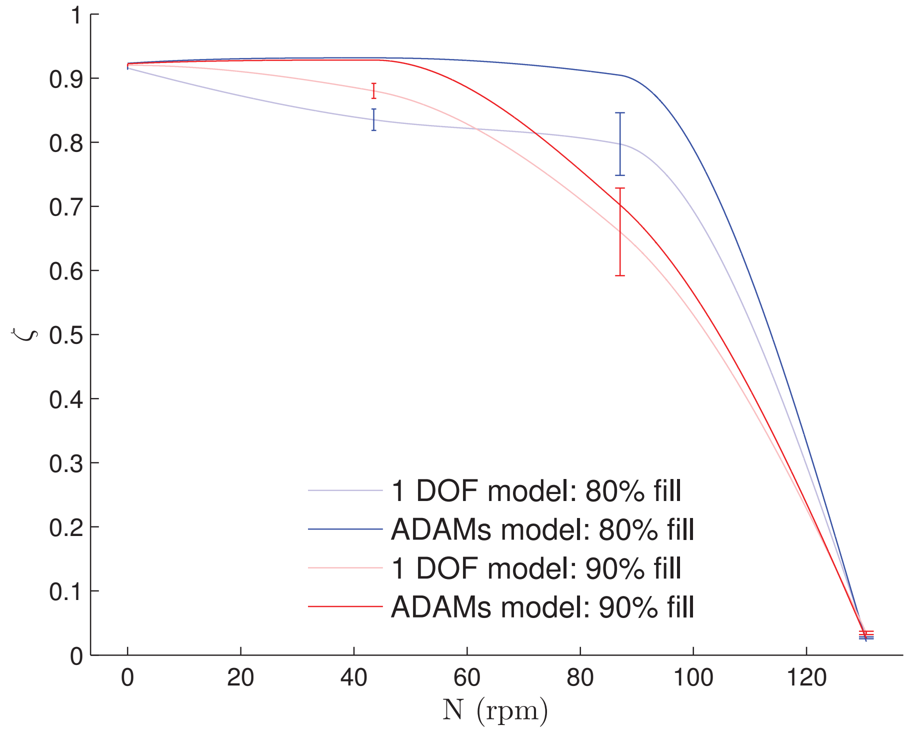

Figure 4–9: Modeled vs experimental damping coefficients for iRings.

4.9 The ADAMs Multi-Post Ride Test

In this section, results from the in-silico ADAMS Multi-Post test provide answers to the full vehicle ride performance questions raised in Chapter 1. Section 4.9.1 presents the data as a frequency spectrum while Section 4.9.2 uses weighed rms acceleration.

4.9.1 Power Spectral Density of Vertical Accelerations

This section displays the Power Spectral Density of the responses of the Juno and Artemis rovers when subjected to the ADAMs Multi-Post ride test described in Section 3.4.

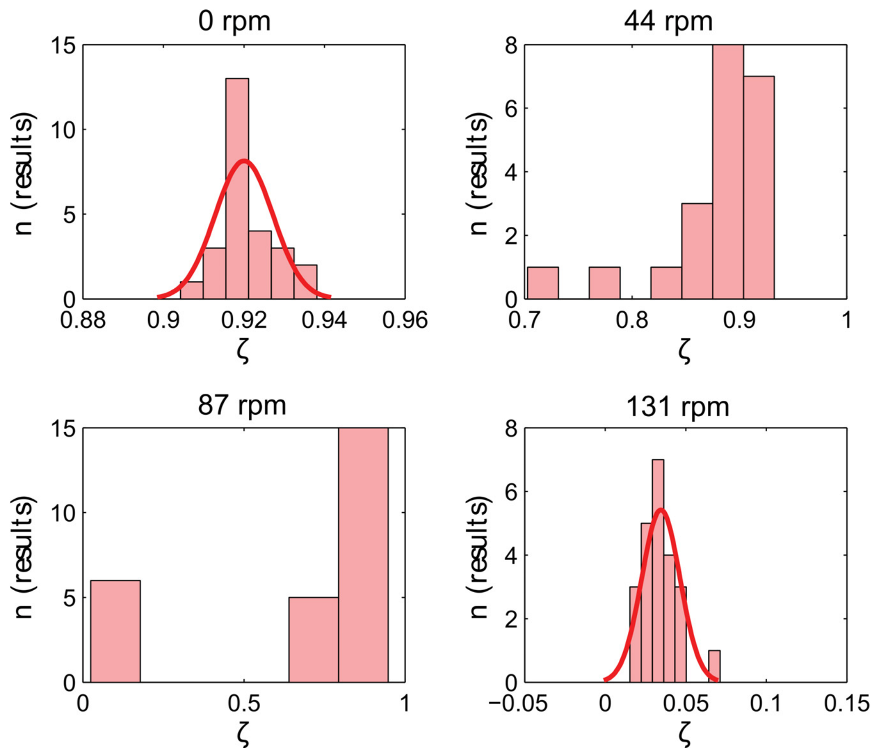

Figure 4–10: Statistical analysis of the 90% filled iRings drop test.

4.9.2 Weighted RMS Accelerations

This section presents the weighted rms accelerations using the methods described in Section 2.2.1.

Table 4–3: Weighted Root Mean Squared Acceleration Rover Response

			Wheel		
			iRings		Rubber
	Rover Mass [Kg]	Speed [Km/hr]	(80%)	(90%)	(7 Psi)
Juno	180	2.5	3.93	4.63	1.57
Artemis	500	4.5	3.46	4.90	0.72
		10	1.37	0.76	0.42
	800	4.5	2.27	3.27	0.72
		10	0.88	0.49	0.42

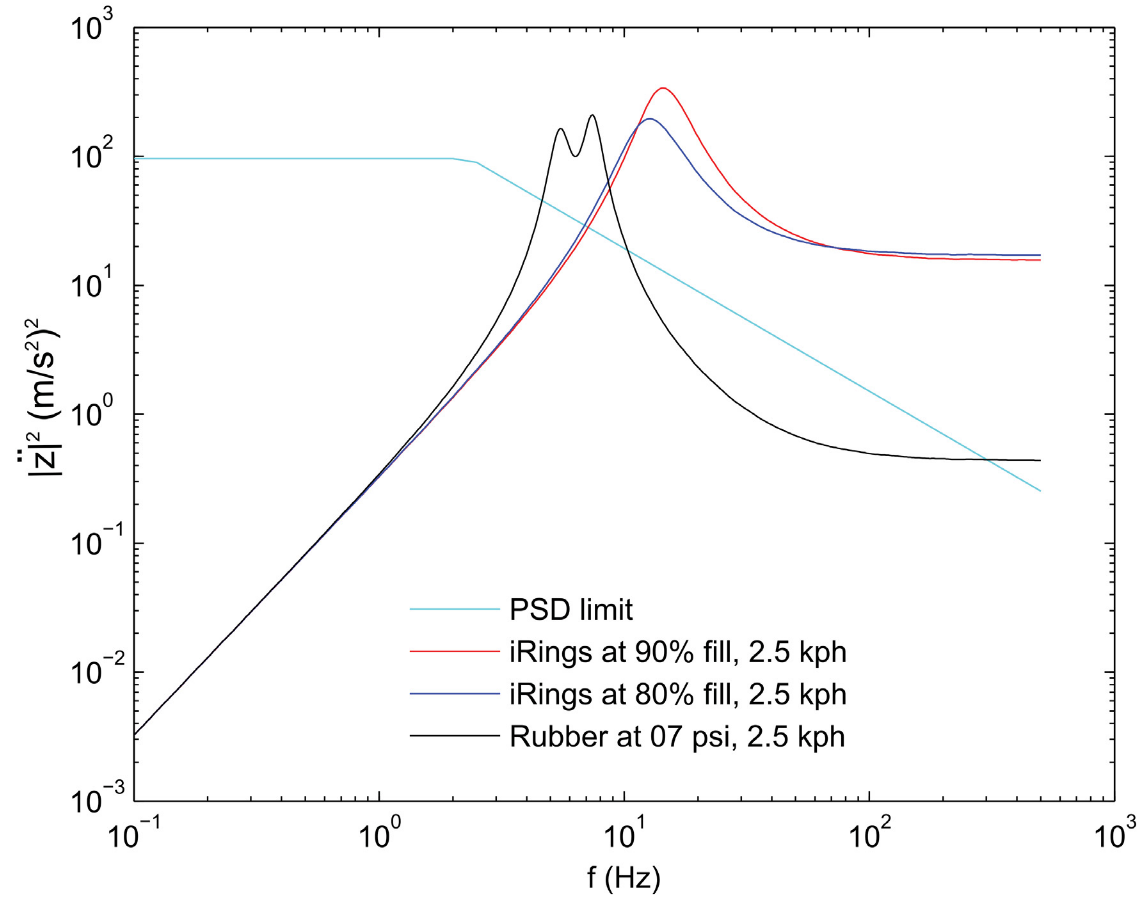

Figure 4–11: Acceleration PSD response of the 180 Kg Juno Rover.

4.10 Conclusions

In closing, the in-situ and in-silico responses of wheels tested alone or as part of the CSA rovers are compared to each other and to comparable data from the literature. The graphical and visual frequency and time domain responses identify trends in ride performance , while derived coefficients c, k, ζ, and the weighted $\ddot{z}_{rms}$, rate them qualitatively. The next chapter examines both types of results

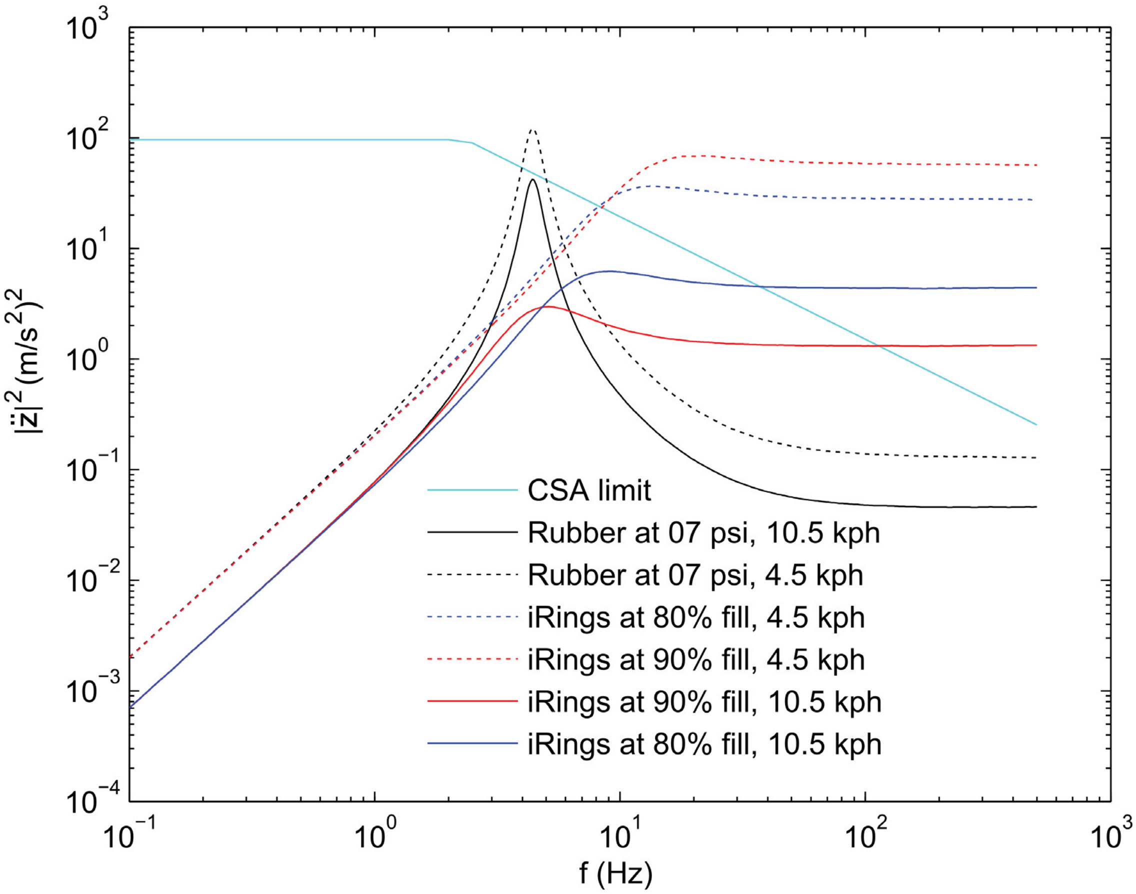

Figure 4–12: Acceleration PSD response of the 500 Kg Artemis Rover.

through the lens of the literature discussed in Chapter 2 to understand the ride performance of iRings and fidelity of the methods used to measure it.

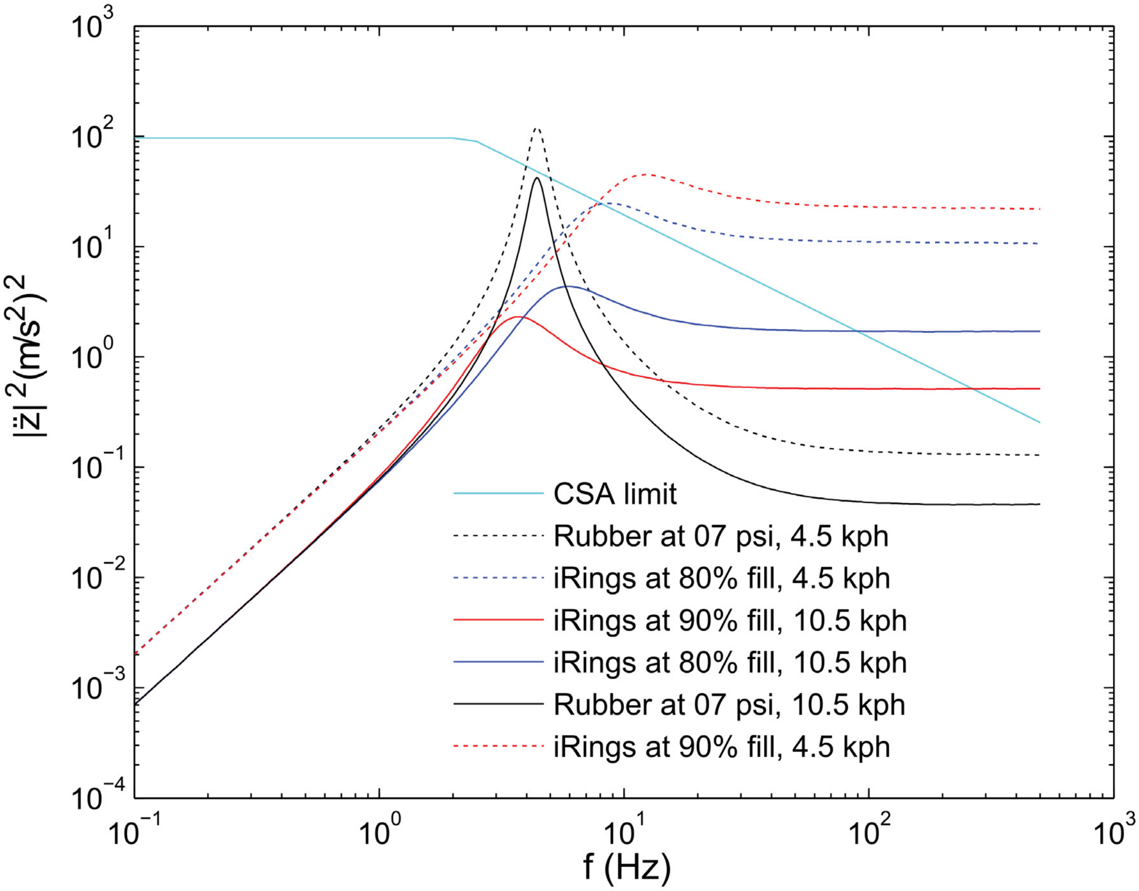

Figure 4–13: Acceleration PSD response of the 800 Kg Artemis Rover.

CHAPTER 5
Discussion

5.1 Introduction

In this chapter, Section 5.2 deals with iRings' ride performance whereas Section 5.3 considers the fidelity of the test methodology.

5.2 Comfort Performance of iRings

In Section 1.5.1 of the introduction, the subject of iRings ride is divided into three questions related to critical speed, angular velocity, and percent fill. These are covered in Sections 5.2.1 to 5.2.3 respectively.

5.2.1 Critical Speed

As illustrated in Figure 1–6, there is a critical speed beyond which the charge solidifies. As discussed in Sections 2.3.1 and 2.3.2, the charge of a mill becomes stiffer, and less dissipative causing its damping ratio to drop as a result (Equation 2.2.12). For a 24 inch mill in earth gravity, Davis (Equation 1.4.1) estimates this speed at 54 rpm. In Section 2.4.1, Martins adds that at this transition speed, measures of charge energy and entropy, to which c, k and ζ are related, are briefly discontinuous.

In Figure 5–2, iRings' damping ratios drop two orders of magnitude near the speed predicted by Davis when filled to 90%. Furthermore, the probability distributions of the 90% and 80% fill damping ratios, in Figs. 4–10 and B–1 respectively, flatten noticeably between 44 and 87 rpm: a sign of a transition.

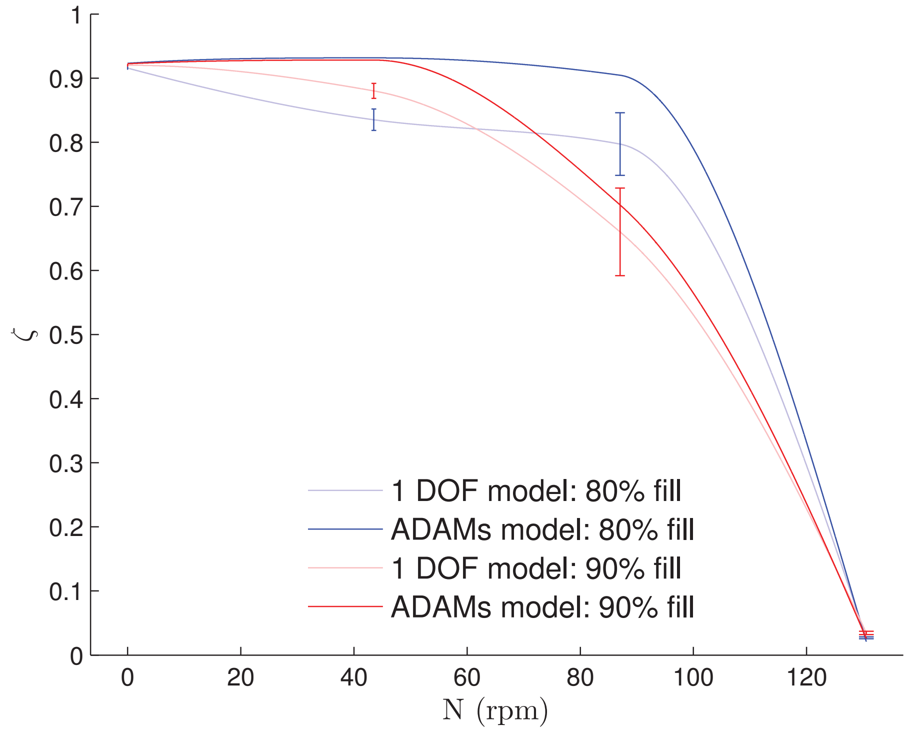

Figure 5–2: Modeled vs experimental damping ratio coefficients for iRings.

5.2.2 Angular Velocity

As speed is increased, the damping coefficient diminishes gradually from 0 to 87 rpm before increasing by two orders of magnitude at 131 rpm to 0.05 kN-s/m as summarized in Table 4–1. In the frequency spectra, a narrowing of peaks both for the 90% filled wheel (Figs. 4–6a to 4–6d) and for the 80% filled wheel (Figs. B–2e to B–2h) is present and is a sign of decreased damping.

In Table 4–1, it is observed that stiffness drops off tenfold at 87 rpm for a 90% fill. At 80%, the drop is less pronounced (fivefold) and occurs after 131 rpm. This is confirmed visually by the increased amplitude of oscillation accompanying increased speed in Figs. 4–7 and B–2. As Section 2.2.5 points out, decreasing stiffness is advantageous to ride, provided that the amount of travel is not exceeded.

Unexpectedly, when the spectra for the 90% fill are overlayed (Figure 4–4b) the natural frequency at all speeds converge to a value of 3-4 hz. The 80% filled wheels also converge to 3-4 Hz but less neatly as the spectra are rougher. Surprisingly, the 20 fold decrease in stiffness between 0 and 131 rpm does not cause a 4 to 5 fold increase in natural frequency (Equation 2.2.11. The fact that the oscillations of the in-situ acceleration responses at 131 rpm in Figs. 4–7d and B–2d are not symmetrical about zero leaves little doubt that iRings is indeed non-linear.

One explanation is that a combination of effects in the tire unrelated to elastic energy storage are producing a “quasi-stiffness”. This would also explain why wheel stiffness does not increase at super-critical speeds like the charge of a tumbling mill would. Also, note that due to the extreme decrease in damping, the damping ratio decreases regardless.

Figure 5–3: Video frames of the 80% filled iRings wheel throughout a 131 rpm drop test

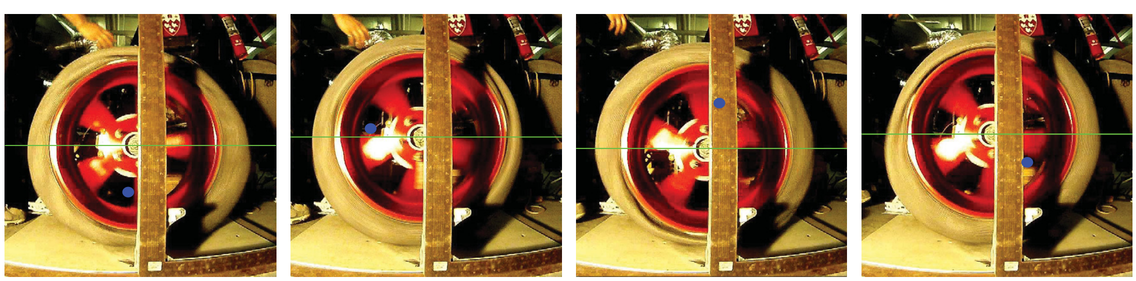

(a) $2/60^{ths}$ sec (b) $9/60^{ths}$ sec (c) $17/60^{ths}$ sec (d) $25/60^{ths}$ sec

In Figure 5–3, the video stills capture two bulges , one on each side of the contact patch, appearing upon impact. These are smoothed out by the wheel as it spins at 131 rpm (2.2 Hz), causing it to hit two lumps per rotation and thus appearing to oscillate at 4 Hz with a peak to peak amplitude of $\sim$1 inch. Pneumatic wheels can produce similar oscillation but it is due to a small mass imbalance produced by wear, manufacturing defects, or non-concentric installation exceeding 2 mm [2]. While such plastic deformation would be irreversible on a metallic non-pneumatic wheel, iRings demonstrates the unique ability to re-harden itself into a circular shape from the action of rolling.

At 0 and 44 rpm, the tire exhibits rebound resembling reversible energy storage. While the video footage is too slow to observe the 44 rpm oscillation, the 0 rpm oscillations makes it clear a non-rolling form of compliance is present. Granular Elasticity (Section 2.3.1), reliant upon material deformation just like continuum materials, is one possibility. Reynolds Dilatancy may provide a second explanation. As explained in Section 2.3.2, if a granular material is sufficiently consolidated, it can dilate when sheared, which in the case of iRings, may allow it to push back against deformation.

5.2.3 Percent Fill

The interpolated trend between ζ and wheel rpm in Figure 5–2 shows that an increase in fill from 80% to 90% reduces the critical speed from $\sim$ 90 rpm to $\sim$ 50 rpm. This indicates that Watanabe's critical speed relationship (Equation 2.4.2) may be valid for iRings, thought it's 15% predicted decrease of critical speed is three times too small.

Furthermore, according to the Davis equations estimate of critical speed, in lunar gravity the change in dynamics properties - perhaps even a change in granular phase [23] - would occur at 2.5 km/hr for a 90% filled wheel, exactly in the middle of its operating speed range of 0 to 5 km/hr.

The current iRings design shines less brightly with respect to damping ratio ζ. The super-critical values of ζ range from 0.9 to 0.8, which is a little high and the super-critical value of 0.01 is much too low relative to Genta's optimal value of 0.354 (Section 2.2.3).

Decreasing fill does little to help, causing only a minor drop in ζ at sub-critical speeds. Rose and Sullivan's dimensional analysis for tumbling mills (Equation 2.4.1) which predicts higher damping, and therefore higher ζ, runs opposite to this.

At the vehicle level, the weighted rms accelerations of the pneumatic wheel values are less than half of those for iRings except at 90% fill on Artemis at 5 and 10 km/hr. The pneumatic tire is always within the comfort limits while the iRings wheel falls outside the limits at the lower speed of 4.5 km/hr but not at 10.5 km/hr. Figures 4–11 to 4–13 identify strong attenuation near resonance but poor attenuation for inputs above 10 Hz as the cause. As Section 2.2.3 points out, this can be resolved by simply reducing damping.

The next section offers some solutions based on observations of the current materials and methods.

5.3 Methodology Fidelity

As underscored in Chapter 3, the iRings model is pivotal in determining the fidelity of the ADAMs Multi-Post ride test. Hence, this section dedicates Section 5.3.1 the rolling drop test and Section 5.3.2 to the implementation of the LSDOF model in ADAMs.

5.3.1 The Rolling Drop Test

Based on the values in Table 4–2, the AT-489 bears the most resemblance to a car tire although it still has double the compliance and a damping ratio twice as high. Given the paucity of off-road tire values in the literature, this result is qualitative at best.

As for the independence of the individual test runs, the probability distributions of the damping ratios at 0 and 131 rpm in Figs. 4–10 and B–1 vaguely resemble Gaussian distributions.

5.3.2 The LSDOF Model Implementation in ADAMs

The fit of the LSDOF to the time-domain response and the shape of the frequency response of the AT-489 in Figs. 4–6 and 4–6 support the accuracy of the RDT in dealing with linear systems. However, it must be noted the duration of accelerometer data are only a fifth of the tire's response; the other four seconds of the readings are dropped as the tire does not maintain contact with the ground which is one of the experimental assumptions.

The LSDOF model of iRings has mixed results in the time domain. At 0 rpm, and 44 rpm, the model captures the first peak but not those that follow. There is oscillation at 0 rpm, but it only lasts for less than a quarter of a second. At 131 rpm, it successfully captures the oscillation but not the peak acceleration. This is not entirely the fault of the model as the oscillations are not symmetric about zero at this speed. At 87 rpm, the model adequately captures both the peak and the oscillations that follow. Oddly, this is the speed with the most uneven Gaussian distribution of damping coefficients.

In the frequency domain, the 87 rpm data is the closest fit. The ADAMs model fits the data up until 15 Hz at 44 rpm and 87 rpm but not at 131 rpm. Additionally, at 131 rpm the model has a natural frequency of 2 Hz instead of 4 Hz which was found experimentally. This is a good considering that Captain et al [56] report that a point-follower tire contact model overestimates the predicted force by 2.5 times in the 1-10 Hz region and 3.5 times in the 10-100 Hz region. For a preliminary ride test, this is sufficient as it covers the most sensitive range of the human body: 4-8 Hz.

Finally, the in-silico damping ratios agree well with the experimental ones in Figure 4–9 with all but those at 44 rpm falling within the confidence intervals of the in-situ values.

5.4 Conclusions

Drawing on the literature review for context, the results from the previous chapter reveal iRings has a straightforward damping coefficient but an unusual and non-linear quasi-stiffness at some operating speeds. Despite this twist, the LSDOF model performs well enough in the time and frequency domains to set a course for further optimization of the wheel. The AT-489 results confirm to an acceptable degree the independence and accuracy of the test methods used here, albeit for a linear system. The following chapter reformulates these results to answer the six principal thesis questions.

CHAPTER 6
Conclusions

6.1 Introduction

The goal of this research is to complete a ride analysis of a particulate filled wheel. In order to complete such an analysis, a number of questions need to be answered. However, in order to answer these questions, a few objectives need to be met. These objectives and a summary of the results obtained are summarized in Section 6.2. Additionally, Section 6.3 recommends improvements to the materials and methods and Section 6.4 draws the thesis to a close with some final words about iRings.

6.2 Thesis Questions

This section revisits the six questions posed at the close of the introduction to this thesis.

Question 1-1: If particles are tumbled in a chain-mail cylinder as opposed to a rigid one, will they exhibit a critical speed? If so, how close is it to the speed predicted by the Davis equation?

The iRings wheel displays a critical speed and this appears to be influenced by radius and gravity much like a tumbling mill. When filled to 90%, the wheel reaches critical around 50 Hz in terrestrial gravity (Figure 5–2), 4 Hz shy of Davis' estimation (Equation 1.4.1).

Question 1-2: Beyond critical speed, do stiffness and damping change in a manner advantageous to ride?

The iRings wheel decreases its damping beyond the critical speed, just like a mill would, which improves ride according to Uys et al [34]. Stiffness decreases with speed and this can be beneficial provided wheel travel increases sufficiently to prevent bottoming out.

Question 1-3: Can the charge of iRings be used to adjust it's parameters enough to meet the ride requirements specified by the CSA?

Damping ratio, and to a lesser degree natural frequency, both require adjustment but fill appears to change neither of these. What it does change is critical speed, but as stated in the discussion, this already finds itself in an acceptable range.

Question 2-1: What is the fidelity of the iRings model?

Its frequency response is sufficiently close to the experimental values in the most sensitive range of the human body, 4-8 Hz, except at 131 rpm. Its in-silico damping ratios meanwhile are within the confidence limits of the in-situ values except at 44 rpm.

Question 2-2: What is the fidelity of the rover models?

The rover models used in the ADAMs Multi-Post simplify the vehicle in three ways. Firstly, the it is pared down to its chassis and its bogies whose geometry and density are chosen to remain true to the vehicle's mass, wheelbase and track width. Secondly, since the position of the payload, human or otherwise, is not given, it is incorporated into the mass of the chassis. Thirdly, the iRings and AT-489 wheels are both set to 5 Kg while for the Multi-Post test so as to eliminate the effect of wheel inertia on the rover bogies.

Question 2-3: What is the fidelity of the in-silico terrain inputs and ride measurements?

The terrain is represented by a string of sinusoids whose temporal frequencies are ordered from lowest to highest and whose amplitudes are defined by the quadratic PSD functions in Table 3–4. This assumes the vehicle speed is constant, that the elevation profile is smooth and symmetric vertically. Identical terrain signals are communicated on either side of the rover via vertical wheel inputs whose phases are made a function of their longitudinal position to capture vehicle speed. This neglects the role of geometric wheel filtering and assumes the terrain does not differ significantly along the width of the vehicle.

Ride is measured at the center of mass of the vehicle and considers only the vertical acceleration component. This provides enough information to optimize the ride of iRings, but amounts to an underestimate as it neglects rotational accelerations.

6.3 Recommendations

The following subsections offer suggestions for improving the Rolling Drop Test, the LSDOF model and the ADAMs Multi-Post ride test.

6.3.1 The Rolling Drop Test

As for the research materials, a more slippery "landing" surface for the wheel may permit rolling drop tests of rubber tires which could help isolate the systematic error introduced by friction. This surface could also be used for a rolling test of the iRings wheel while in contact with the ground to determine what amount of oscillation is attributed to simply rolling. Adding instantaneous torque readings using strain gauges on the drive shaft could also help determine damping independently by measuring rolling resistance.

With the present data, parameters for a Hunt and Crossley model, introduced in Section 2.3.1, could also be derived numerically provided the exponents of position and velocity do not exceed 3-4. Based on the authors experience with ADAMs, higher values make the ODE's too stiff for the solver.

Another idea would be to measure position and from it, derive a displacement transfer function. This could be done with linear or rotational encoders or even with image processing software provided the frame rate of the camera could be increased by an order of magnitude to several hundred fps.

6.3.2 The LSDOF Model

As a start, more tests in the 44 to 87 rpm range would clarify how the damping ratio behaves as it transitions through the critical speed.

Furthermore, model fidelity could almost be doubled by replacing the point-follower with an in series filter such as the Rigid-Treadband or Fixed-Footprint models described by Captain et al [56]. Given then potential of iRings for large local deformation, this approach is expected to alter the full vehicle ride results in its favour.

6.3.3 The ADAMs Multi-Post Ride Test

Until full vehicle testing is carried out, there exists no way to validate the data provided by the ADAMs ride tests. One way of getting around this obstacle would be to conduct scaled down tests with the 1/8 scaled micro-rover outfitted with iRings wheels in Figure 6–1 [21].

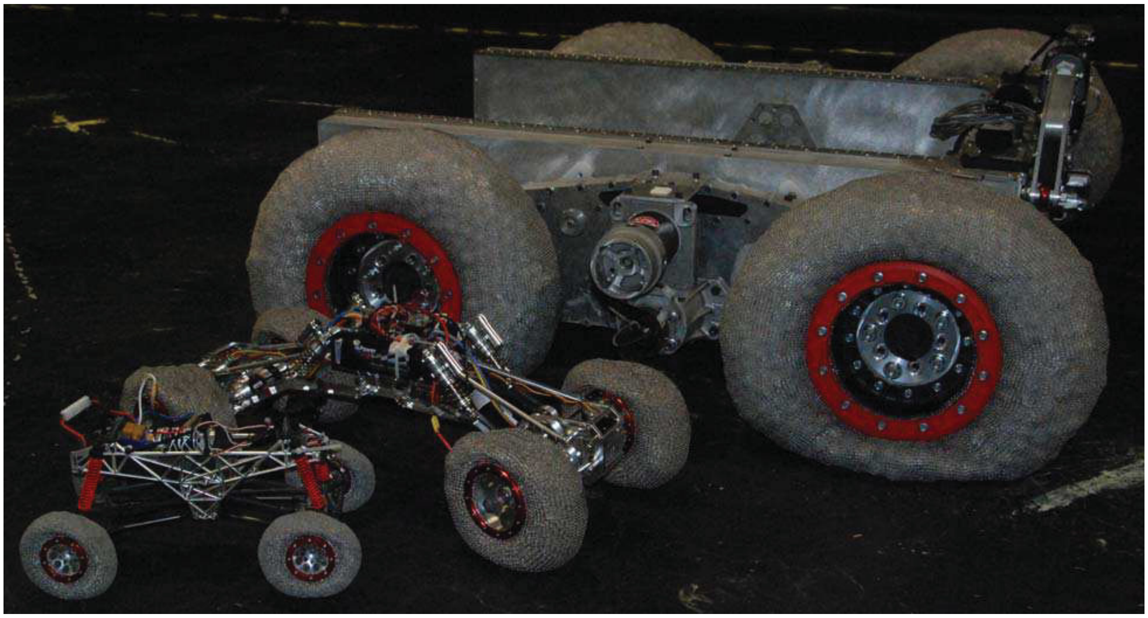

Figure 6–1: Three scales of iRings wheels [21]. From left: 1/5 th, 1/8 th and full scale.

6.4 Final Words

In summary, iRings shows promise as a passively adaptive suspension component but better analytical and physical tools are necessary to understand how to optimize it. Moreover, its design is simple, robust and temperature insensitive.

It is uncertain that it will meet the high frequency requirements set out by the CSA. This is not a wholly unsurprising result since the particulate wheel is presently only a proof of concept design. Given the opportunity, there is a good chance that this class of wheel, or one derived from it, can meet the general requirements. A further design iteration is therefore strongly suggested. This will leverage the lessons learned, for both the wheel and the testing procedure, and has the potential to produce an improved wheel.

Thompson's pneumatic tire, remained a curiosity for forty years. It was Dunlop who's pairing of it with another fledgling technology - the bicycle - sparked a revolution in transportation. Similarly, what this curious particle filled wheel named iRings needs most is not optimization, but opportunity.

Appendices

APPENDIX A
Detailed Materials and Methods

This appendix offers detailed information about the materials and methods introduced in Chapter 3. Appendix A.1 relates how the iRings model is developed while Appendix A.2 provides information on the ADAMs Multi-Post ride test.

A.1 Rolling Drop Test

This section provides details on the materials used in the in-situ Rolling Drop Test (RDT) pictured in Figure A–1. These include the McGill Baja, the proximity sensor, the accelerometer, the c-RIO and the Go-Pro camera. Appendix A.1.1 offers a detailed description of the materials and Appendix A.1.2 provides information on their calibration.

A.1.1 Detailed Test Description

Onto a purpose built wood fixture are mounted the Mini-Baja and a sheet of High Density Polyethylene (HDPE). The sheet of HDPE is screwed to the frame below the rear-right wheel. The Baja is clamped to an elevated section of the fixture. The shock absorber is removed, allowing the suspension to articulate freely. A rope mounted to an a-arm and a pulley on a boom mounted to the frame are used to raise the wheel.

The Baja chassis is elevated such that when either iRings or the AT-489 hit the ground, the wheel plane is vertical and so is the axis of the accelerometer.

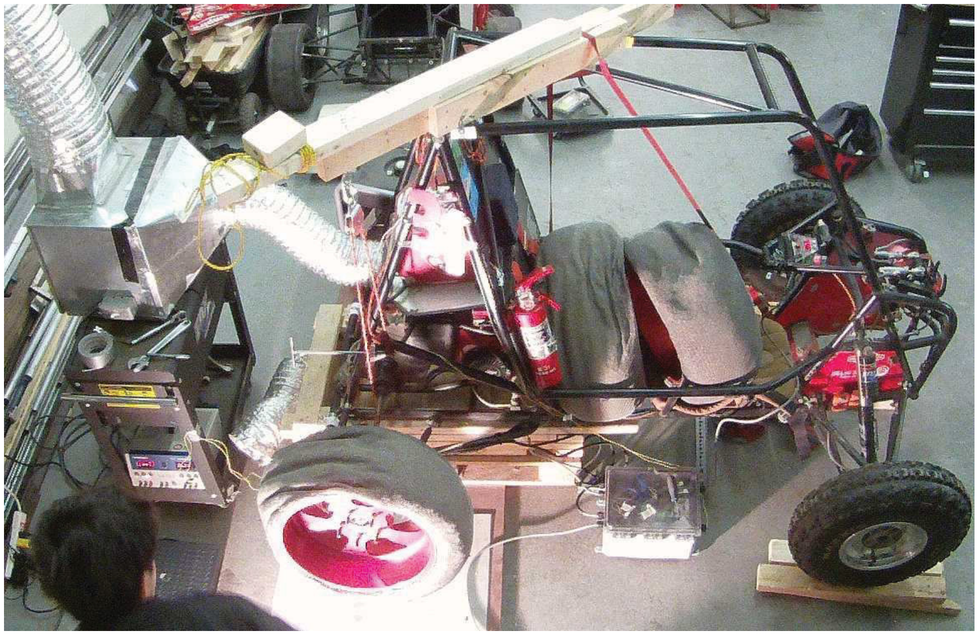

Figure A–1: The Mini Baja rolling drop-test rig - top

A magnetic proximity sensor (model GS100502) made by *Cherry* is mounted to the wheel-hub to measure angular velocity. A three-axis seat-pad accelerometer, originally purchased for full vehicle testing of iRings and the Mini-Baja, is re-purposed as a vertical accelerometer. It is removed from its rubber enclosure and mounted with double sided tape to the top a-arm.

A Tri-Axial ICP seat pad accelerometer (mode l356B41) made by *PCB Piezotronics* is certified for use in whole body vibration studies in accordance with ISO ride standard 2631. The accelerometer readings are scaled using the ratio between the acceleration normal to the accelerometer and the vertical acceleration measured at the center of gravity of the wheel.

For the rolling drop-test, the accelerometer was removed from the rubber seatpad and mounted to the drop test using double sided tape which is a non-standard usage. Judging by the accurate capture of gravity in free-fall, the effect on accuracy is assumed to be negligible. Also, the most convenient mounting point for the accelerometer was offset from the center of mass of the iRings wheel. To compensate, acceleration measurements are taken at the accelerometer position and the iRings center of mass to produce the appropriate gain as shown in Figure A–2.

A $go-pro^{tm}$ camera is aimed to face the side of the wheel. An led light is placed in the foreground. The light, connected to the C-RIO, lights up at the moment recording begins, allowing the video footage to be synchronized with the data. See Appendix XX for instrumentation details.

A.1.2 Rolling Drop Test Calibration

This section details the calibration of the speed, acceleration measurements and drop height of the RDT.

The c-RIO's processor converts the hall-effects sensor readings into an equivalent forwards speed in kph assuming a wheel diameter of 24 inches and no slip. The result is output in real-time to a digital display with ±0.1 accuracy. Using the readout, the engine throttle position is calibrated for ”speeds” of 5,10 and 15 km/h (44, 87 and 131 rpm).

The accelerometer readings must be calibrated to account for it being placed away from the center of mass of the wheel. Acceleration measurements at these two positions, found using the in-silico RDT, are shown in Figure A–2. The average ratio between the two measurements while in free-fall, 1.2626, serves as the accelerometer gain for the in-situ experiment.

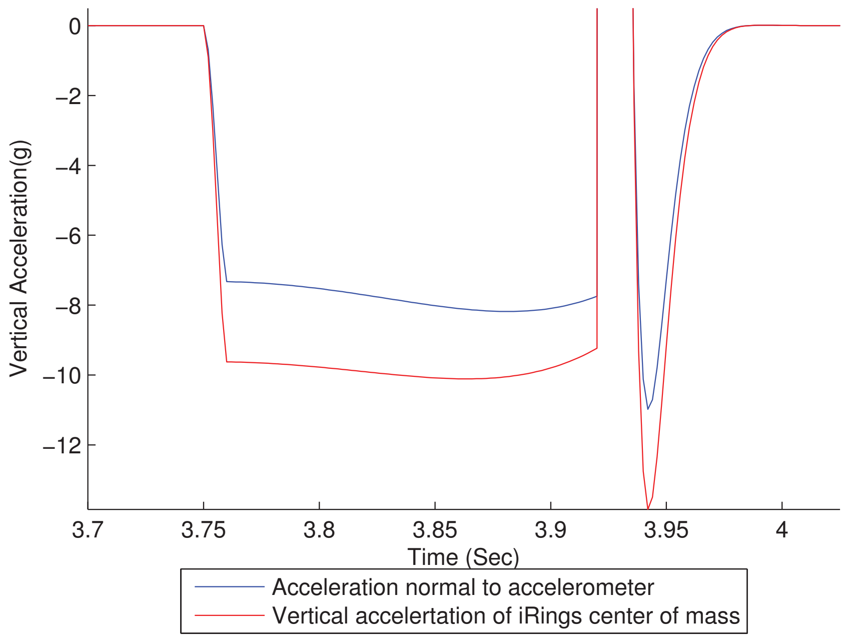

Figure A–2: Comparison of acceleration measurements during free-fall

The drop height of the RDT must be sufficient to excite the modes in the first 25Hz of the frequency reseponse. The textbook definition of the useful frequency range is that which falls below the cutoff frequency. This value is where the amplitude of the frequency response falls below 10-20 dB of the peak value [57].

A.2 The ADAMs Multi-Post Ride Test

In the ADAMS simulations the symmetric H-shaped Artemis has no defined front end while the front end of Juno is the open side of the C-shaped frame. In Juno, acceleration measurements are taken at the midpoint between the axles of the left and right walking beams. On Artemis, the acceleration measurements are

Table A–1: Drop test parameters

wheel	Fill	Response time	Speed	Damping Coefficient	Damped Natural Frequency	Time constant	Settling time $(4 \cdot \tau)$	Cutoff Frequency (-10db)
				ζ	ω_d	τ	T_s	ω
		(sec)	rpm		(hz)	(sec)	(sec)	(hz)
iRings	80%	2	0	0.92	3.6386	$3.67 \cdot 10^{-}3$	0.0147	39.6
			44	0.8767	3.8656	$7.10 \cdot 10^{-}3$	0.0284	42.7
			87	0.6602	3.2610	$1.06 \cdot 10^{-}2$	0.0425	48.2
			131	0.0346	3.9859	0.715	2.86	25.9
iRings								
	90%	2	0	0.9156	3.6292	$3.66 \cdot 10^{-}3$	0.0146	44.6
			44	0.8350	4.0385	$5.20 \cdot 10^{-}3$	0.0208	34.4
			87	0.7971	3.3428	$2.27 \cdot 10^{-}2$	0.0908	56.0
			131	0.0269	3.9859	0.576	2.30	31.86
Pneumatic (AT-489)	7 Psi	1.3	0	0.1669	7.862	5.9	0.236	NA

taken at the geometric center of the plane defined by the four walking beam axles. The measurement point on each vehicle is the location of two constraints called "joint primitives" in ADAMS. One prevents rotation about z, or yaw; the other prevents movement in x and y.

It is only possible to tune the pitch of the Juno rover by altering the length of the connecting differential linkage. The Juno suspension is configured in this thesis to have a horizontal chassis on flat ground. On Artemis, suspension tuning via adjustment of torsional spring preload can alter wheel load distribution. The Artemis suspension is configured in this thesis with a spring rate of 1000 kN/m and a preload chosen to equalize ground pressure at all eight wheels on flat ground.

To simulate the effect of forward motion while the vehicle is stationary, the actuator inputs are offset in time.

$$\theta(deg) = \omega \left(\frac{rad}{sec}\right) \cdot \Delta t(sec) \cdot 360 \left(\frac{degrees}{2\pi\, radians}\right) \tag{A.2.1}$$

$$\Delta t = \frac{wheel\, base(m)}{vehicle\, forwards\, velocity(m/s)} \tag{A.2.2}$$

$$\tag{A.2.3}$$

APPENDIX B
Supplemental Wheel Characterization Results

This Appendix provides the data obtained from the methods described in Sections 3.2 to 3.4 of the methodology. These were omitted from Chapter 4 due to their resemblance to the results of the 90% filled wheel.

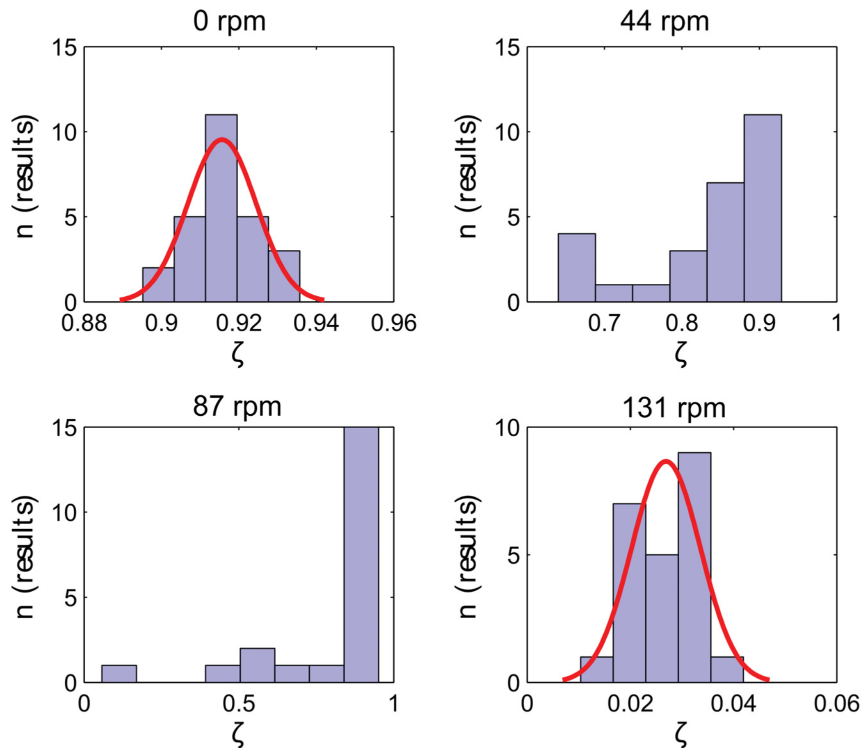

Figure B–1: Statistical analysis of the 80% filled iRings drop test.

Figure B–2: 80% Filled iRings Time Domain Response for 0, 44, 87 and 131 rpm Rolling Drop Test and LSDOF Model

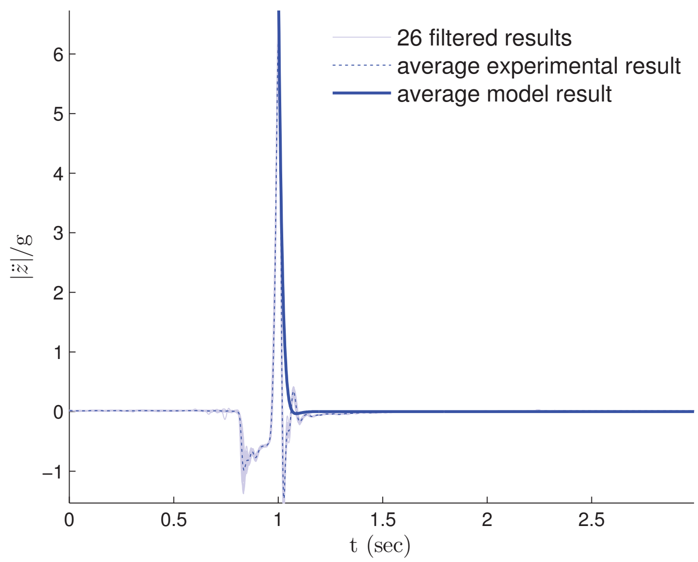

(a) 0 rpm

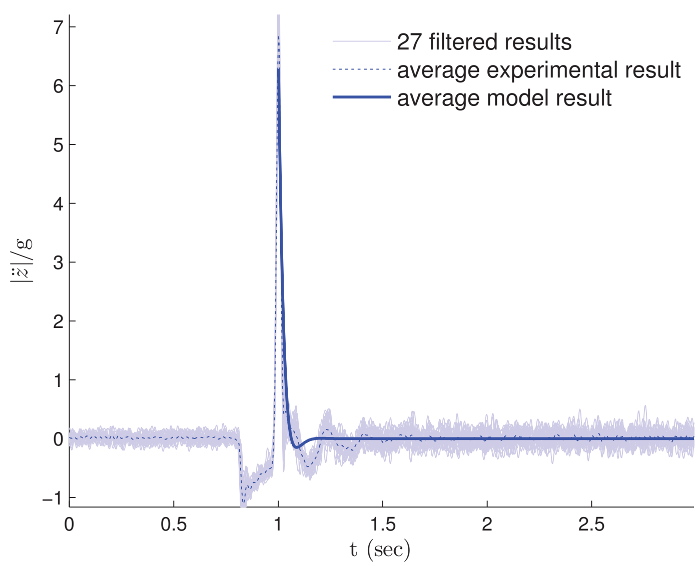

(b) 44 rpm

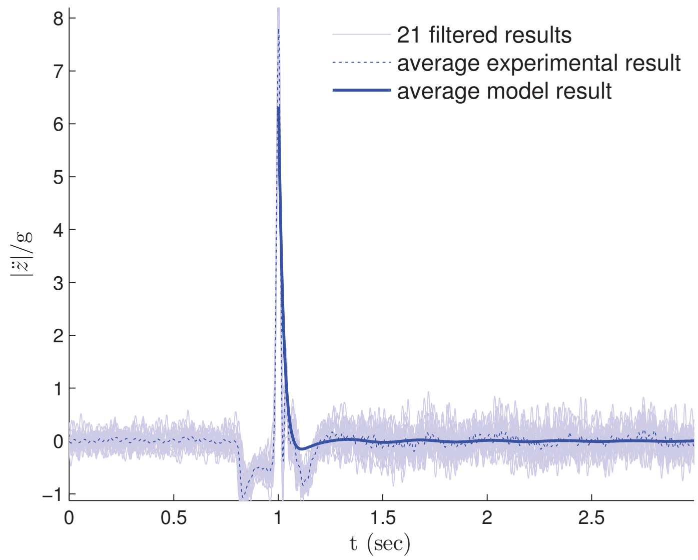

(c) 87 rpm

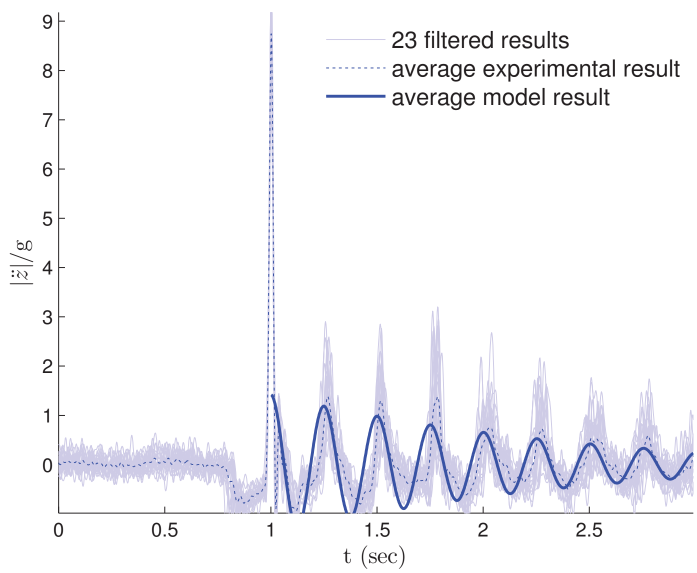

(d) 131 rpm

Figure B–2: 80% Filled iRings Time Domain Response to 0, 44, 87 and 131 rpm Rolling Drop Test

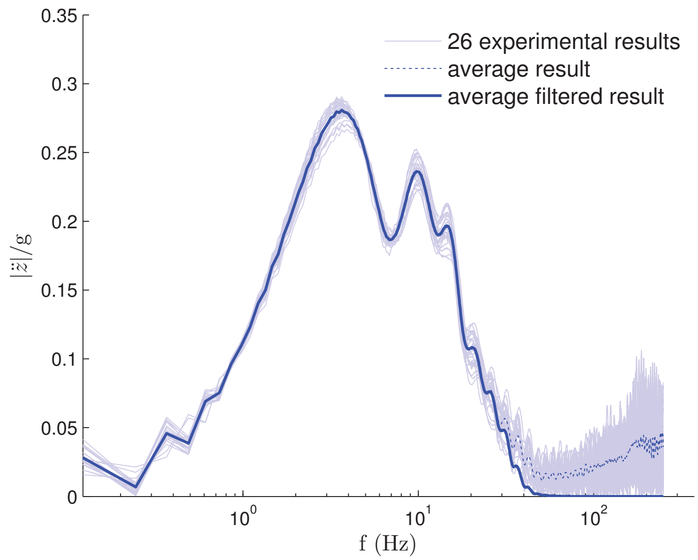

(e) 0 rpm

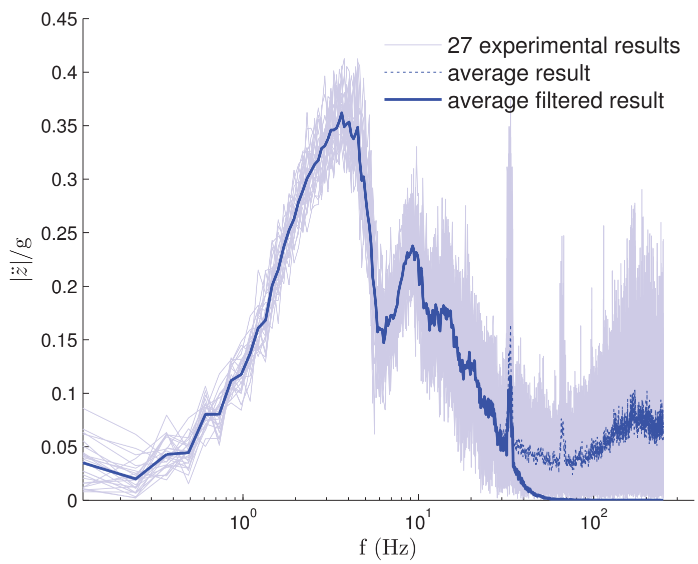

(f) 44 rpm

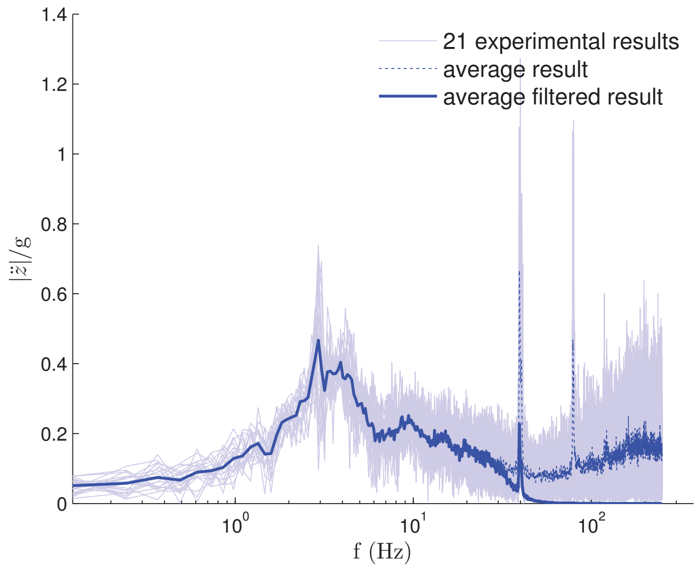

(g) 87 rpm

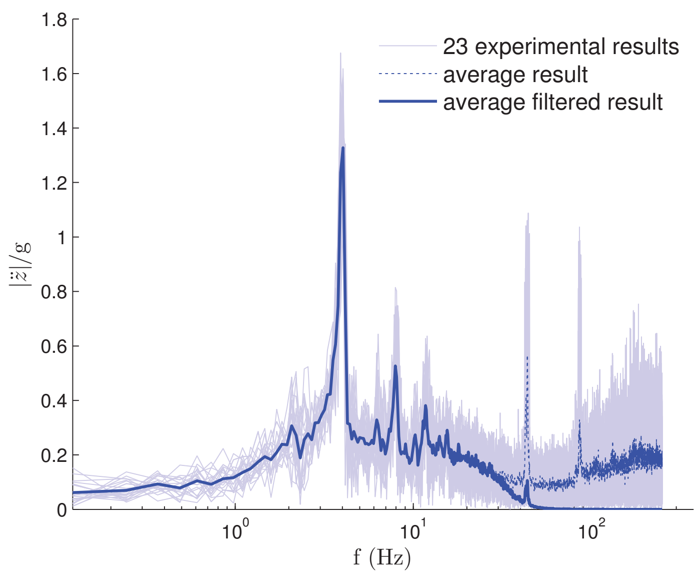

(h) 131 rpm

Figure B–3: Comparison of 80% Filled iRings Frequency Domain Response to 0,44, 87 and 131 rpm In-Situ and In-Silico Rolling Drop Tests

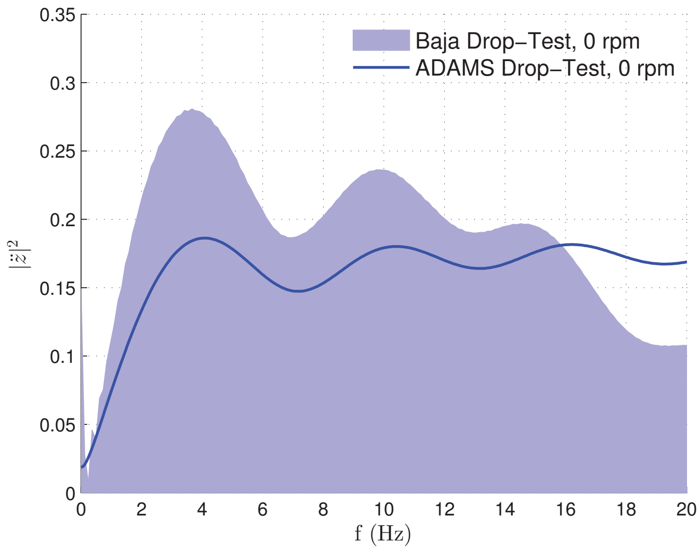

(a) 0 rpm Response

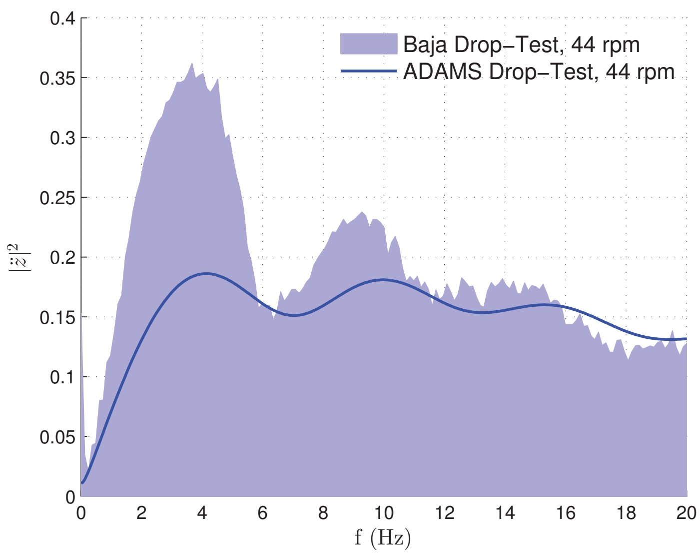

(b) 44 rpm Response

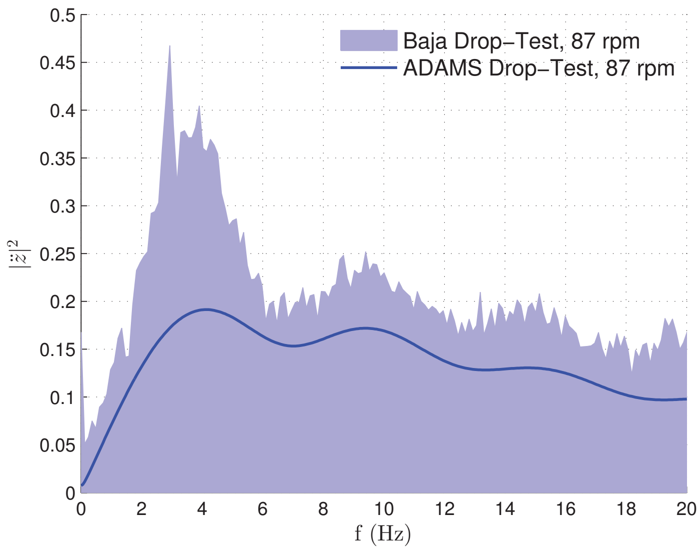

(c) 87 rpm Response

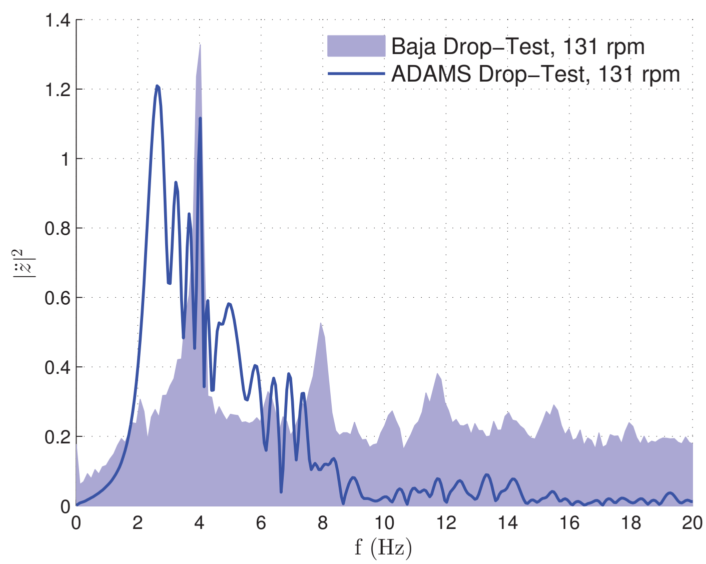

(d) 131 rpm Response

References

[1] G. Shearer, "The rolling wheel - the development of the pneumatic tyre," in *Proceedings of the Institution of Mechanical Engineers*, vol. 191, no. 1. SAGE Publications, 1977, pp. 75–87.

[2] H. Heisler, *Advanced Vehicle Technology*. Elsevier Science, 2002. [Online]. Available: http://books.google.ca/books?id=aLgNET9YkS0C

[3] A. Young, *Lunar and planetary rovers: the wheels of Apollo and the quest for Mars*, ser. Springer-Praxis books in space exploration. Springer, 2007. [Online]. Available: http://books.google.ca/books?id=Q92nGnDBMX0C

[4] NASA, "Apollo program summary report: Synopsis of the apollo program activities and technology for lunar exploration," National Aeronautics and Space Administration (NASA), Tech. Rep. JSC-09423, 1975. [Online]. Available: http://hdl.handle.net/2060/19750013242

[5] R. Mueller, "Nasa human spaceflight architecture team: Lunar surface exploration strategies," in *Global Space Exploration Conference*, 2012.

[6] J. George, G. Mattes, K. Rogers, D. Magruder, A. Paz, H. Vaccaro, R. Baird, G. Sanders, J. Smith, J. Quinn *et al.*, "Resolve mission architecture for lunar resource prospecting and utilization," in *Lunar and Planetary Institute Science Conference Abstracts*, vol. 43, 2012, p. 2583.

[7] P. Visscher, D. Boucher, M. Picard, J. Smith, and N. Cristello, "Artemis jr. rover mobility platform," in *Aerospace Sciences Meetings*. American Institute of Aeronautics and Astronautics, Jan. 2013, pp. –.

[8] Artemis jr rover. Neptec Design Group. Accessed June 17th 2013. [Online]. Available: http://www.neptec.com/brochures/Artemis-Jr-Rover.pdf

[9] NASA, *Lunar Roving Vehicle Operations Handbook Appendix A (Performance Data)*, 1971. [Online]. Available:

http://www.lpi.usra.edu/lunar/documents/NTRS/collection2/NASA_TM_X_66816.pdf

[10] V. Asnani, D. Delap, and C. Creager, “The development of wheels for the lunar roving vehicle,” *Journal of terramechanics*, vol. 46, no. 3, pp. 89–103, 2009.

[11] Exploration Surface Mobility Project, “Prototype lunar exploration light rover requirements,” Canadian Space Agency, Exploration Surface Mobility Requirements Document CSA-ESM-RD-0004 Revision A, 2010.

[12] G. Heiken, *Lunar sourcebook: a user’s guide to the moon*, 2nd ed. Cambridge Univ Pr, 1991.

[13] A. Young, *Chapter 1: From Concept to Reality*, ser. Springer-Praxis books in space exploration. Springer, 2007, ch. Destiny at Taurus-Littrow, p. 205. [Online]. Available: http://books.google.ca/books?id=Q92nGnDBMX0C

[14] C. Bell, “”re: Weights of simplified juno rover”,” Personal E-mails, July 30 2012.

[15] T. Garrett, K. Newton, and W. Steeds, *The motor vehicle*. Society of Automotive Engineers, 2001.

[16] B. D. Harrington and C. Voorhees, “The challenges of designing the rocker-bogie suspension for the mars exploration rover,” in *37th Aerospace Mechanisms Symposium, May 19-21, 2004, Johnson Space Center, Houston, Texas*. Pasadena, CA: Jet Propulsion Laboratory, National Aeronautics and Space Administration, 2004, 2004.

[17] P. Bartlett, “Kinematic suspension design for planetary surface vehicles,” Ph.D. dissertation, Carnegie Mellon University, 2008.

[18] Anon, “Apollo 14 technical crew debriefing,” NASA Manned Spacecraft Center, Tech. Rep., 1971.

[19] The Goodyear Tire and Rubber Company, “Tire comprising springs and method of manufacturing a tire,” European Patent EP 2 386 430 A1, 1999.

[20] P. Radziszewski and S. Martins, “A particulate filled fabric wheel,” U.S. Patent 20120223497 A1, Sept. 6 2009.

[21] P. Radziszewski, S. Martins, M. Faragalli, N. Kaveh-Moghaddam, D. Oyama, R. Briend, N. Gharib, C. Prahacs, S. Ouellette, D. Pasini *et al.*, "iringsdevelopment of a wheel prototype concept for lunar mobility," *Canadian Aeronautics and Space Journal*, vol. 57, no. 1, p. 11, 2011.

[22] D. Oyama and P. Radziszewski, "irings wheel endurance test plan and results," October 2011, juno rover test report.

[23] S. Martins, "Exploring tumbling mill dynamics through sensor development," Ph.D. dissertation, McGill University, 2012.

[24] J. C. Dixon, *The Shock Absorber Handbook*, 2nd ed. Wiley, 2007.

[25] J. Lackner and P. DiZio, "Human orientation and movement control in weightless and artificial gravity environments," *Experimental Brain Research*, vol. 130, no. 1, pp. 2–26, 2000.

[26] ISO, *Mechanical Vibration and Shock: Evaluation of Human Exposure to Whole-body Vibration. Part 1, General Requirements: International Standard ISO 2631-1: 1997 (E).* ISO, 1997.

[27] M. Blundell and D. Harty, *The Multibody Systems Approach to Vehicle Dynamics*, ser. Automotive Engineering Series. Elsevier Science, 2004. [Online]. Available: http://books.google.ca/books?id=3GnIfH6K5GEC

[28] G. Genta and L. Morello, *Comfort Performance*, ser. Mechanical Engineering Series. Springer Netherlands, 2009, pp. 349–428. [Online]. Available: http://dx.doi.org/10.1007/978-1-4020-8675-5_10

[29] J. Wong, *Theory of Ground Vehicles*. John Wiley & Sons, 2008. [Online]. Available: http://books.google.ca/books?id=Blp2D1DteTYC

[30] F. Sugasawa, H. Kobayashi, T. Kakimoto, Y. Shiraishi, and Y. Tateishi, "Electronically controlled shock absorber system used as a road sensor which utilizes supersonic waves," *SAE Paper*, vol. 851652, 1985.

[31] B. Bachrach and E. Rivin, "Pneumatic damping of vehicle tires to improve ride quality," SAE, Tech. Rep., 1984.

[32] B. S. Kim, C. H. Chi, and T. K. Lee, "A study on radial directional natural frequency and damping ratio in a vehicle tire," 2007.

[33] E. I. Rivin, “Pneumatic wheels,” Patent, April 1999, uS-5891278. [Online]. Available: http://www.patentlens.net/patentlens/patent/US_5891278/en/

[34] P. Uys, P. Els, and M. Thoresson, “Suspension settings for optimal ride comfort of off-road vehicles travelling on roads with different roughness and speeds,” *Journal of Terramechanics*, vol. 44, no. 2, pp. 163 – 175, 2007. [Online]. Available: http://www.sciencedirect.com/science/article/pii/S0022489806000474

[35] Y. Jiang and M. Liu, “Granular elasticity without the coulomb condition,” *Phys. Rev. Lett.*, vol. 91, p. 144301, Sep 2003. [Online]. Available: http://link.aps.org/doi/10.1103/PhysRevLett.91.144301

[36] J. Geng, D. Howell, E. Longhi, R. Behringer, G. Reydellet, L. Vanel, E. Clément, and S. Luding, “Footprints in sand: the response of a granular material to local perturbations,” *Physical Review Letters*, vol. 87, no. 3, p. 35506, 2001.

[37] P. visualisation of stresses in an assembly of disks. Photoelastic visualisation of stresses in an assembly of disks. Delft University of Technology. Accessed July 19th 2013. [Online]. Available: http://dutcgeo.ct.tudelft.nl/allersma/diskshear.htm

[38] L. Ding, Z. Deng, H. Gao, K. Nagatani, and K. Yoshida, “Planetary rovers wheelsoil interaction mechanics: new challenges and applications for wheeled mobile robots,” *Intelligent Service Robotics*, vol. 4, pp. 17–38, 2011, 10.1007/s11370-010-0080-5. [Online]. Available: http://dx.doi.org/10.1007/s11370-010-0080-5

[39] G. Gilardi and I. Sharf, “Literature survey of contact dynamics modelling,” *Mechanism and Machine Theory*, vol. 37, no. 10, pp. 1213 – 1239, 2002. [Online]. Available: http://www.sciencedirect.com/science/article/pii/S0094114X02000459

[40] D. Krimer, M. Pfitzner, K. Bräuer, Y. Jiang, and M. Liu, “Granular elasticity: General considerations and the stress dip in sand piles,” *Physical review E*, vol. 74, no. 6, p. 061310, 2006.

[41] K. Sakaie, D. Fenistein, T. J. Carroll, M. van Hecke, and P. Umbanhowar, “Mr imaging of reynolds dilatancy in the bulk of smooth granular flows,” *EPL (Europhysics Letters)*, vol. 84, no. 3, p. 38001, 2008.

[42] M. Kuhn, M. Nakagawa, R. Oliver, B. Scarlett, F. Radjai, R. A. Williams, M. Massoudi, P. Evesque, D. Scott, S. Biggs, S. Simons, R. Dave, U. Tuzun, J. M. Rotter, J. Zhu, S. Edwards, D. Grinev, M. J. Hounslow, A. D. Salman, G. K. Reynolds, C. F. W. Sanders, D. W. York, R. Jones, C. S. Hodges, H. Troadec, S. Roux, P. Pagliai, T. G. Sitharam, S. V. Dinesh, and B. R. S. Murthy, *Granular Materials*, S. J. Antony, W. Hoyle, and Y. Ding, Eds. The Royal Society of Chemistry, 2004. [Online]. Available: http://dx.doi.org/10.1039/9781847550996

[43] H. Pacejka, *Tyre and vehicle dynamics.* Butterworth-Heinemann, 2006. [Online]. Available: http://books.google.ca/books?id=wHlkbBnu9FEC

[44] D. Newland, *An introduction to random vibrations and spectral analysis.* Longman, 1984. [Online]. Available: http://books.google.ca/books?id=MQBRAAAAMAAJ

[45] M. Feldman, *Hilbert Transform Applications in Mechanical Vibration.* Wiley, 2011. [Online]. Available: http://books.google.ca/books?id=SrxInm2Kz_IC

[46] A. Wheeler and A. Ganji, *Introduction to Engineering Experimentation.* Pearson Higher Education, 2009. [Online]. Available: http://books.google.ca/books?id=crppr4QT068C

[47] S. Najafabadi, J. Kövecses, and J. Angeles, "A comparative study of approaches to dynamics modeling of contact transitions in multibody systems," in *a.* ASME, 2005.

[48] S. Park, A. Popov, and D. Cole, "Influence of soil deformation on off-road heavy vehicle suspension vibration," *Journal of terramechanics*, vol. 41, no. 1, pp. 41–68, 2004.

[49] J. Zakrajsek, D. McKissock, J. Woytach, J. Zakrajsek, F. Oswald, K. McEntire, G. Hill, P. Abel, D. Eichenberg, and T. Goodnight, "Exploration rover concepts and development challenges," in *1 st Space Exploration Conference: Continuing the Voyage of Discovery.* Citeseer, 2005, pp. 1–23.

[50] Exploration Surface Mobility Project, "Rover to payload interface requirements document (ird)," Canadian Space Agency, Exploration Surface Mobility Requirements Document CSA-ESM-RD-0004 Revision B, 2010.

[51] ISO, *Mechanical Vibration and Shock: Evaluation of Human Exposure to Whole-body Vibration. Part 1, General Requirements: International Standard ISO 2631-1: 1985 (E).* ISO, 1985.

[52] M. Sayers and S. Karamihas, *The little book of profiling: basic information about measuring and interpreting road profiles*, 1998. [Online]. Available: http://www.instrumentationdevices.com/images/upload/2010_8_8_14_13_50_littlebook98r.pdf.pdf

[53] R. J. Pike and W. J. Rozema, "Spectral analysis of landforms," *Annals of the Association of American Geographers*, vol. 65, pp. 499–516, 1975.

[54] B. Jones, P. Visscher, D. Boucher, P. Radziszewski, M. Faragalli, S. Spenler, and D. Apostolopoulos, "The juno rover: an extraction vehicle for in-situ resource utilization," in *Proceedings of the 15th CASI Astronautics Conference ASTRO*, vol. 2010, 2010.

[55] Goodyear, "Goodyear newsroom image gallery," Online database, accessed July 2013, accessed 2012/11/23. [Online]. Available: http://www.goodyear.com/cfmx/web/mediaphotos/

[56] K. M. CAPTAIN, A. B. BOGHANI, and D. N. WORMLEY, "Analytical tire models for dynamic vehicle simulation," *Vehicle System Dynamics*, vol. 8, no. 1, pp. 1–32, 1979. [Online]. Available: http://www.tandfonline.com/doi/abs/10.1080/00423117908968566

[57] R. Dukkipati, *Mechanical Vibrations.* Morgan & Claypool, 2010. [Online]. Available: http://books.google.ca/books?id=VM1ePgAACAAJ